A&A, 699, A344 (2025)
https://doi.org/10.1051/0004-6361/202554736
© The Authors 2025

Astronomy & Astrophysics

Two neighbours of the ultra-short-period Earth-sized planet K2-157 b in the warm Neptunian savanna⋆

A. Castro-González[1,⋆⋆], F. Bouchy[2,3], A. C. M. Correia[4,5], A. Sozzetti[6], J. Lillo-Box[1], P. Figueira[2,7], B. Lavie[2], C. Lovis[2], M. J. Hobson[2], S. G. Sousa[7,8], V. Adibekyan[7,8], M. R. Standing[9], N. C. Hara[3,10], D. Barrado[1], A. M. Silva[7,8,11], V. Bourrier[2], J. Korth[12], N. C. Santos[7,8], M. Damasso[6], M. R. Zapatero Osorio[1], J. Rodrigues[7,8,13], Y. Alibert[14,15], S. C. C. Barros[7,8], S. Cristiani[16], P. Di Marcantonio[16], J. I. González Hernández[17,18], G. Lo Curto[19], C. J. A. P. Martins[7,20], N. J. Nunes[11], E. Palle[17,18], F. Pepe[21], A. Suárez Mascareño[17,18], and H. M. Tabernero[22,23]

(Affiliations can be found after the references)

Received 25 March 2025 / Accepted 25 April 2025

ABSTRACT

Context. The formation and evolution of ultra-short-period (USP) rocky planets is poorly understood. However, it is widely thought that these planets could not have formed at their present-day close-in orbits, but instead migrated inwards through interactions with outer neighbours.

Aims. We aim to confirm and characterise the USP Earth-sized validated planet K2-157 b ($P_{\rm orb}$ = 8.8 h) and constrain the presence of additional companions in the system through radial velocity (RV) measurements.

Methods. We measured 49 RVs with the ESPRESSO spectrograph and tested different planetary and non-planetary configurations to infer the model that best represents our data set. We derived the orbital and physical properties of the system through a global RV and transit model.

Results. We detected two additional super-Neptune-mass planets located within the warm Neptunian savanna, K2-157 c ($P_{\rm orb,c} = 25.942^{+0.045}_{-0.044}$ d, $M_{\rm p,c} \sin i = 30.8 \pm 1.9$ $M_\oplus$) and K2-157 d ($P_{\rm orb,d} = 66.50^{+0.71}_{-0.59}$ d, $M_{\rm p,d} \sin i = 23.3 \pm 2.5$ $M_\oplus$). The joint analysis constrains the mass of K2-157 b at the 2.7σ level, $M_{\rm p,b} = 1.14^{+0.41}_{-0.42}$ $M_\oplus$ (<2.4 $M_\oplus$ at 3σ), which, together with the inferred radius, $R_{\rm p,b} = 0.935 \pm 0.090$ $R_\oplus$, make the planet compatible with a rocky composition with a likely (68% confidence) higher iron-to-silicate mass fraction than Earth. K2 data discard non-grazing transit configurations for K2-157 c ($i_{\rm c} < 88.4°$ at 3σ), and ESPRESSO data constrain the eccentricities of K2-157 c and K2-157 d to $e_{\rm c} < 0.2$ and $e_{\rm d} < 0.5$ at 3σ. Our dynamical analysis indicates that the system is stable for eccentricities up to $e_{\rm c}$, $e_{\rm d} \sim 0.3$ and mutual inclinations up to ~60°. At a population level, we find that the trend that the closest USP planets tend to orbit late-type stars does not hold when scaling the orbital separation to the Roche limit, which suggests that the orbital distribution of the closest planets across spectral types is primarily determined by tidal disruption.

Conclusions. The orbital architecture of K2-157 is unusual in the known exoplanet plethora, with only one similar case reported to date: 55 Cnc. The USP planets of these systems, being accompanied by massive, long-period, relatively spaced, and possibly misaligned neighbours, could have migrated inwards through eccentricity-based mechanisms triggered by secular interactions.

Key words. techniques: photometric – techniques: radial velocities – planets and satellites: detection – planets and satellites: dynamical evolution and stability – planets and satellites: individual: K2-157 b – stars: individual: K2-157 (EPIC 201130233)

1. Introduction

Ultra-short-period (USP) planets are defined as planets that orbit their host stars in less than one day. Appearing in 0.51 ± 0.07% of G-dwarf stars and 0.83 ± 0.18% of K-dwarf stars (Sanchis-Ojeda et al. 2014), these planets are an unusual outcome of planet formation and evolution. Interestingly, while USP planets have been detected in a wide range of radii and masses, from sub-Earths to super-Jupiters, they generally show terrestrial sizes (i.e. $R_{\rm p} < 2$ $R_\oplus$). Hence, their extremely short orbits offer unique observational advantages that facilitate the characterisation of small planets with Earth and sub-Earth masses. Being subjected to extreme irradiation and gravitational conditions, USPs also allow us to explore physical and chemical phenomena for which there are no analogues in the Solar System.

An Earth-mass USP planet with a half-day orbit around a Sun-like star induces a radial velocity (RV) signal of 80 cm s^{-1}. While apparently small, 0.5-to-1 m s^{-1} planetary signals are within the reach of state-of-the-art spectrographs. In particular, the high-resolution ESPRESSO spectrograph (Pepe et al. 2021), with an on-sky RV precision better than 10 cm s^{-1} on short timescales (<1 h) and of 40 cm s^{-1} in the long term (Figueira et al. 2025), offers an excellent opportunity to characterize the population of small USP planets.

Small USP planets receive insolations thousands of times larger than that received by the Earth, so that any primordial H/He-dominated atmosphere is expected to have been removed through photo-evaporation (e.g. Sanchis-Ojeda et al. 2014; Lundkvist et al. 2016; Lopez 2017; Owen 2019). The masses and radii of small USP planets have thus been directly used to probe their internal structures (e.g. Dai et al. 2019; Guenther

⋆ Based on observations collected at the European Southern Observatory (ESO) under the programmes with IDs 1102.C-0744, 1102.C-0958, 1104.C-0350, and 106.21M2.004.

⋆⋆ Corresponding author: acastro@cab.inta-csic.es

Open Access article, published by EDP Sciences, under the terms of the Creative Commons Attribution License (https://creativecommons.org/licenses/by/4.0), which permits unrestricted use, distribution, and reproduction in any medium, provided the original work is properly cited.
This article is published in open access under the Subscribe to Open model. Subscribe to A&A to support open access publication.

et al. 2024; Murgas et al. 2024; Grieves et al. 2025). Most rocky USP planets have equilibrium temperatures larger than 1800 K, which implies that their rocky mantles are partially molten, forming extensive 'magma oceans' on the side facing the star (e.g. Tikoo & Elkins-Tanton 2017; Dorn & Lichtenberg 2021; Shorttle et al. 2024; Lichtenberg & Miguel 2025). While magma oceans have a negligible impact on the inferred compositions of rocky planets (e.g. Boley et al. 2023), molten rocks have a great storage capacity of volatiles, which can be outgassed, possibly generating secondary high mean-molecular weight atmospheres (e.g. Kite & Barnett 2020; Tian & Heng 2024). Interestingly, USP planets lie inside the stellar Alfvénic sphere, so they are thought to undergo strong magnetic interactions with their host stars. Today, signs of these interactions have been detected in systems with giant planets (e.g. Shkolnik et al. 2005; Cauley et al. 2019; Castro-González et al. 2024c), and next-generation optical and radio instrumentation may open the door to similar detections in low-mass planets (e.g. Bourrier et al. 2018b; Shkolnik & Llama 2018). Small USP planets are also amenable to observations of phase curves and secondary eclipses with the James Webb Space Telescope (JWST; Gardner et al. 2006), which might unveil the presence of secondary atmospheres or the surface mineralogy in bare rocky surfaces (e.g. Hu et al. 2012; Demory et al. 2016; Zhang et al. 2024).

USP planets are known to be affected by strong tidal forces exerted by their host stars, which gradually shrink their orbits, potentially bringing them within the tidal disruption limit. In this region, rocky material can be detached from the planet, even to the point of completely disrupting the whole planet (Rappaport et al. 2013). Orbital decay towards the disruption limit may occur over timescales ranging from millions of years to several gigayears (e.g. Jia & Spruit 2017; Winn et al. 2018; Dai et al. 2024), depending primarily on the orbital separation of the USP planet. In this regard, some authors point out that the disintegrated material would be engulfed by the star, potentially altering its photospheric compositions by a measurable amount (e.g. Ramírez et al. 2015; Oh et al. 2018; Behmard et al. 2023; Liu et al. 2024; Soares et al. 2025), and others have managed to detect the possible disintegration process through strong asymmetries in the transit signals (e.g. Rappaport et al. 2012, 2014; Sanchis-Ojeda et al. 2015; Hon et al. 2025).

While the end-state of the life of small USP planets is fairly well understood, many doubts remain about their origins. The fundamental problem is that it is unlikely that these planets formed at their present-day locations due to the extreme temperatures in these close-in regions (e.g. Boss 1998) and the likely truncation of the proto-planetary disc at much larger distances (e.g. Lee & Chiang 2017). In this regard, while tides can shrink a planetary orbit once a close-in location is reached, they are probably not efficient enough to bring planets to the USP regime within the age of the Universe (e.g. Goldreich & Soter 1966; Winn et al. 2018). An early theory proposed that USP planets are the remnant cores of tidally disrupted migrated giant planets (Jackson et al. 2013, 2016). However, this possibility has been discarded as the predominant mechanism given that hot Jupiters (e.g. Santos et al. 2001) and hot Neptunes (e.g. Vissapragada & Behmard 2025) are found to preferentially orbit metal-rich stars, while the hosts of rocky USP planets show a more solar-like metallicity distribution (e.g. Winn et al. 2017).

The most promising theories of USP planet formation involve high-eccentricity tidal migration (HEM) triggered by secular chaos (Petrovich et al. 2019), low-eccentricity migration due to secular forcing (Pu & Lai 2019), and obliquity-driven tidal migration (Millholland & Spalding 2020). While fundamentally different, these theories converge into a common prediction: small USP planets are brought to their present-day orbits through interactions with outer planetary companions. In this line, the *Kepler* mission (Borucki et al. 2010; Howell et al. 2014) showed that USP planets in multi-planetary systems are common. Based on a homogeneous analysis of ten campaigns of the extended K2 mission, Adams et al. (2021) estimated that all USP planets are expected to have planetary neighbours. In addition, thanks to their transiting nature, *Kepler*-based works enabled the measurement of their mutual inclinations (e.g. Fang & Margot 2012; Figueira et al. 2012; Tremaine & Dong 2012; Fabrycky et al. 2014; Dai et al. 2018; Adams et al. 2021), which is crucial to test formation theories. These large-scale photometry-based surveys are of great value given the wealth of constraints achieved in a short time span. However, their conclusions have to be taken with caution, since they are highly biased towards systems with small mutual inclinations and short-orbit companions due to the loss of non-transiting configurations and typically short temporal observing baselines. In this regard, RV follow-up monitoring of USP-hosting systems is crucial to explore relevant regions of the period-inclination parameter space missed by transit surveys.

In this work, we observed the G9 V star K2-157 (V = 12.792 ± 0.057 mag) with the ESPRESSO spectrograph to confirm and characterize the statistically validated USP Earth-sized planet K2-157 b ($P_{\rm orb}$ = 8.8 h; Mayo et al. 2018) and constrain the presence of additional companions. These observations allowed us to detect two super-Neptune-mass planets in the warm Neptunian savanna and measure the mass of K2-157 b. In Sect. 2, we describe the observations analysed in this work. In Sect. 3, we present our stellar characterisation of K2-157 based on a high-resolution, high-S/N ESPRESSO spectrum. In Sect. 4, we describe our analyses and results. In Sect. 5, we discuss the results, and we summarise and conclude in Sect. 6.

2. Observations

2.1. K2 high-precision photometry

K2-157 (EPIC 201130233) was observed by K2 (Howell et al. 2014) in Campaign 10 (C10) from 13 July 2016 (JD 2 457 582.61) to 20 September 2016 (JD 2 457 651.69) in the so-called long-cadence mode (i.e. 29.4 min cadence). We accessed and downloaded the data through the Mikulski Archive for Space Telescopes (MAST)[1]. Between JD 2 457 589.3 and JD 2 457 604.3, there was a failure in a detector (module 4) that caused a data gap of 15 d, resulting in a lower than usual observing time of 54 d. The loss of two reaction wheels caused the spacecraft to undergo continuous drifts that translated into larger systematic errors than those observed in the primary mission. We thus used the `everest` pipeline[2] (Luger et al. 2016, 2018) to correct for instrumental systematics based on the pixel-level decorrelation technique (PLD; Deming et al. 2015). In addition, we downloaded the K2SFF photometry based on the self-flat fielding technique (SFF; Vanderburg & Johnson 2014). We analysed the K2 photometry (Sect. 4.4) by considering both corrections and found consistent results within 1σ. We opted to present the results based on the `everest` correction, but we highlight that the properties of this system do not depend on the correction pipeline. Mayo et al. (2018) analysed WIYN/NESSI speckle and archival images to ensure that no nearby sources are

[1] https://archive.stsci.edu
[2] Available at https://github.com/rodluger/everest

contaminating the photometric aperture. We extended this analysis by searching for nearby *Gaia* DR3 (Gaia Collaboration 2023) sources and found that the nearest star is located 20″ away from K2-157 with a *G* magnitude of 20.4 mag (*Gaia* DR3 3596379973268959744), which ensures a negligible contamination, in agreement with Mayo et al. (2018). Therefore, no additional dilution correction was necessary. In Table B.1, we present the `everest` photometry used in this work.

We computed the transit least squares periodogram (`TLS`; Hippke & Heller 2019)[3] of K2 C10 data to determine the significance of K2-157 b and potentially unveil additional transits. We first detrended the photometry through the bi-weight technique as implemented in `wotan`[4] (Hippke et al. 2019). We generated 14 light curves considering a wide range of window lengths, between 0.2 and 1.5 d (step size of 0.1 d), to ensure that we avoided possible detrending systematics related to the K2-157 b transit duration or orbital period, which could bias the `TLS` analysis. The resulting time series show standard deviations between 134 and 147 ppm (parts per million). The maximum power peaks correspond to the periodicity of K2-157 b (0.365 d) and emerge with signal detection efficiencies (SDE) between 26.0 and 28.1, which are well above the commonly considered thresholds for a significant transit detection (i.e. SDEs from 6 to 10; Siverd et al. 2012; Dressing & Charbonneau 2015; Livingston et al. 2018; Wells et al. 2018). In Fig. A.1, we show the periodogram of the detrended time series with the largest SDE for K2-157 b (corresponding to a window length of 0.5 d). We masked the eclipses of K2-157 b and re-computed the `TLS` periodograms, finding no additional significant peaks.

2.2. TESS high-precision photometry

The Transiting Exoplanets Satellite Survey (TESS; Ricker et al. 2014) observed K2-157 (TIC 349445372) in Sector 46 (S46) from 3 December 2021 (JD 2459551.56) to 30 December 2021 (JD 2459578.70) with a 2-min cadence. We downloaded the available data products from MAST. At the mid-sector, there is a gap of 3 d due to the satellite repointing towards the Earth to downlink the data, resulting in a total observing time of 25 d. We used the PDCSAP photometry, which is the pixel-calibrated simple aperture photometry (SAP) corrected from instrumental systematics by the PDC algorithm (Smith et al. 2012; Stumpe et al. 2012; Jenkins et al. 2016). Given the larger TESS pixel scale than Kepler's (i.e. 21″ vs. 3.98″) and the consequent larger probability of flux contamination, we used the `TESS-cont` algorithm[5] (Castro-González et al. 2024b) to quantify the flux fraction from nearby sources falling within the photometric aperture. We find that 99.7% of the flux comes from K2-157, ensuring negligible contributions from nearby sources. We present the PDCSAP of K2-157 in Table B.2.

We computed the `TLS` periodogram of the PDCSAP, which we detrended similarly to the K2 data (i.e. bi-weight method with a window length of 0.5 d). The resulting time series has a standard deviation of 3574 ppm (or 982 ppm in 30-min bins), which is seven times larger than that in K2's data. We show the periodogram in Fig. A.1. No peak is found with SDE > 7, indicating that the TESS data is not precise enough to detect K2-157 b and that no additional transit signals are detected.

2.3. ESPRESSO high-resolution spectroscopy

We observed K2-157 with the echelle spectrograph for rocky exoplanets and stable spectroscopic observations (ESPRESSO; Pepe et al. 2021), which is mounted on the Very Large Telescope (VLT) located at ESO's Paranal Observatory. These observations were carried out in the context of the Guaranteed Time Observations (GTOs) of the instrument, which previously allowed us to characterize dozens of small rocky planets detected by TESS (e.g. Barros et al. 2022; Damasso et al. 2020; Sozzetti et al. 2021; Demangeon et al. 2021; Castro-González et al. 2023; Damasso et al. 2023; Lavie et al. 2023; Suárez Mascareño et al. 2024; Hobson et al. 2024; Rodrigues et al. 2025) and K2 (e.g. Mortier et al. 2020; Toledo-Padrón et al. 2020; Passegger et al. 2024). We acquired 49 spectra between 19 February 2019 and 19 April 2021 (programme IDs 1102.C-0744, 1102.C-0958, 1104.C-0350, and 106.21M2.004) with a typical cadence of 2-3 d and exposure times between 900 and 1200 s. Given the moderate brightness of the star, we conducted all observations through a single VLT unit in the slow-readout high-resolution mode (HR21), which allowed us to get high-S/N spectra with spectral resolutions of 140 000 across the 380–788 nm wavelength coverage. During the observations, simultaneous calibration was conducted by illuminating a second fibre connected to the instrument with a Fabry-Pérot interferometer (Perot & Fabry 1899) to control environmental changes (Wildi et al. 2010).

We used the ESPRESSO Data Reduction Software (DRS; version 3.3.0)[6] to extract the calibrated spectra and associated RVs. The RV extraction is based on the technique presented by Baranne et al. (1996), whereby the average line profile (or cross-correlation function; CCF) is extracted using a mask weighted according to the RV content (i.e. line depth and sharpness; Bouchy et al. 2001; Pepe et al. 2002). For K2-157, we chose the G9 pipeline mask to obtain the CCFs, which were fitted to a Gaussian profile to compute the wavelength shifts. The relative RVs between the instrument and K2-157 were finally converted into stellar RVs by subtracting the barycentric Earth radial velocity (BERV) and correcting for secular acceleration. The RVs of K2-157 have a median uncertainty of 1.5 m s^{-1} and a standard deviation of 6.2 m s^{-1}. This RV scatter widely exceeds the exquisite ESPRESSO on-sky RV performance (e.g. Suárez Mascareño et al. 2020; Faria et al. 2022; González Hernández et al. 2024; Figueira et al. 2025) and cannot be explained through the small measured uncertainties, suggesting the existence of planetary or stellar signals. The DRS also computes different activity indicators based on the average line profile (i.e. FWHM, BIS, and Contrast of the CCF) and the emission of individual lines particularly sensitive to stellar activity (i.e. H_α, Ca-index, S-index, Na-index, and log R'_{HK}). We additionally used the novel template-matching (TM) algorithm `sbart`[7] (Silva et al. 2022) to get an independent RV extraction, which we note that it is not affected by the recently identified systematic bias in TM algorithms given the large baseline of the observations (Silva et al. 2025). In this work, we opted to present the results based on the CCF RVs and ensured that they are independent of the extraction pipeline (i.e. consistent at 1σ and similar uncertainties). In Table B.3, we present the ESPRESSO data set.

[3] Available at https://github.com/hippke/tls
[4] Available at https://github.com/hippke/wotan
[5] Available at https://github.com/castro-gzlz/TESS-cont
[6] The latest version of the ESPRESSO Data Reduction Software can be found at https://www.eso.org/sci/software/pipelines
[7] Available at https://github.com/iastro-pt/sBART

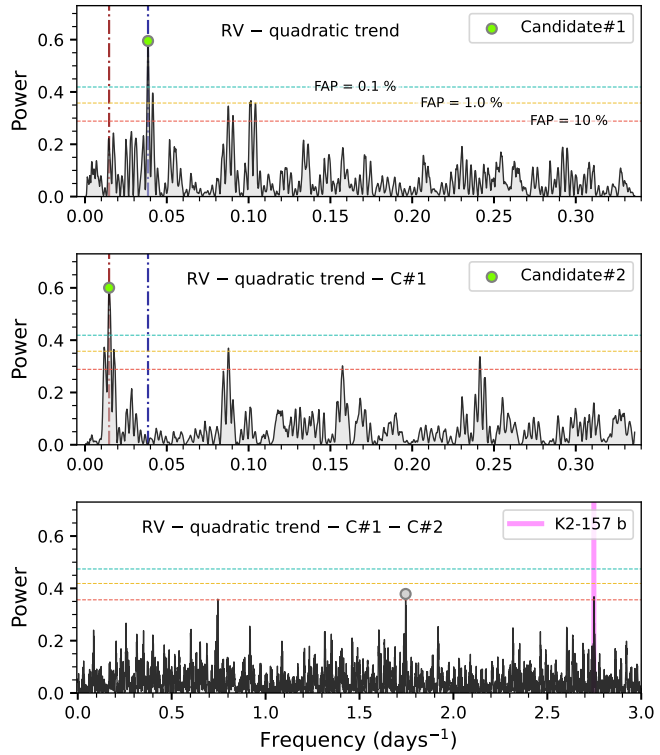


Fig. 1. Generalized Lomb-Scargle periodograms of the ESPRESSO RVs of K2-157 after subtracting a quadratic trend (upper panel) and the RV signals of Candidate#1 (C#1; middle panel) and Candidate#2 (C#2; lower panel). The circles indicate the maximum power frequencies and are highlighted in green when they correspond to a significant signal (FAP < 0.1%).

We computed the generalised Lomb-Scargle periodogram (GLS; Zechmeister & Kürster 2009)[8] of the ESPRESSO RVs and activity indicators to identify sinusoidal signals that could be attributed to planets or stellar activity. The periodogram of the RVs shows its maximum peak at a frequency of 0.03852 d^{-1} (periodicity of 25.96 d) with a False Alarm Probability (FAP) of 1.8×10^{-3}%, which is below the commonly used threshold for considering that a signal is significant (FAP < 0.1%). When subtracting a quadratic trend previously fit to the data through least squares, the maximum power peak remains at this periodicity and its FAP decreases down to 2.5×10^{-5}%. In the upper panel of Fig. 1, we show this periodogram. In the middle panel of the same figure, we show the periodogram of the quadratically detrended RVs subtracted from the 25.96-d sinusoidal signal. A new significant peak pops up at a frequency of 0.014725 d^{-1} (67.91 d) and a FAP of 1.8×10^{-5}%. After subtracting this second signal from the RV data set, no additional significant peaks appear (see the lower panel of Fig. 1). However, we can appreciate three peaks that reach the 10% FAP level[9]. One of these peaks has a frequency of 2.7478 d^{-1} (0.36 d), which perfectly coincides with the orbital period of K2-157 b. The other peaks have frequencies of 1.7455 d^{-1} (0.57 d) and 0.7449 (1.34 d). Overall, while not significant, the appearance of a tentative peak (FAP < 10%) with a 0.36 d periodicity after subtracting the two significant signals suggests that the RV signature of K2-157 b is embedded in our data.

To assess whether the two significant RV signals could have a planetary origin or be contaminated by the activity of the host star, we computed the periodograms of the six activity indicators extracted by the DRS (Fig. A.2). No statistically significant peaks (FAP < 0.1%) appear in any of the indicators, either at the RV frequencies or at any other frequency. To try to unveil possible dependencies between the RVs and activity indicators, we searched for linear correlations through the Pearson correlation coefficient (Rodgers & Nicewander 1988). We find coefficients $r < 0.3$ for all indicators (Fig. A.3), which is considered to reflect negligible correlations. This absence of evident stellar signals suggests that the prominent RV signals correspond to two additional planets in the system. We thus hereinafter refer to the RV signals as planet candidates: Candidate#1 (25.96 d) and Candidate#2 (67.91 d). We note that, while not significant, the periodogram of the H_α indicator shows a relatively prominent peak at 36.9 d with a FAP of 0.26%, making it an interesting candidate to reflect the stellar rotation period, which we further explore in Sect. 4.3.

We also used the ℓ_1 periodogram technique by Hara et al. (2017) and checked that the phase, amplitude, and frequency of Candidate#1 and Candidate#2 are consistent. The ℓ_1 periodogram technique is based on a sparse recovery technique called the basis pursuit algorithm (Chen et al. 1998). It aims to find a representation of the RV time series as a sum of a small number of sinusoids whose frequencies are in the input grid. It outputs a figure which has a similar aspect as a regular periodogram, but with fewer peaks due to aliasing. The peaks can be assigned a FAP, whose interpretation is close to the FAP of a regular periodogram peak, but which takes into account the correlated noise following Delisle et al. (2020). First, the ℓ_1 periodogram takes several parameters as input, in particular a list of vectors, or predictor, which are fitted linearly along with the search for periodic signals. Second, it needs an assumed covariance model, which can be non-diagonal to account for correlated noise. For the base model, we chose an offset and a linear and quadratic trend. We selected the covariance model following Hara et al. (2020): we considered a grid of values for the noise model, and ranked them with cross-validation and Bayesian evidence, computed with the Laplace approximation. In Fig. A.4, we show the ℓ_1 periodogram corresponding to the highest ranked model. The peaks at 25.9 d and 69.3 d are significant, with FAP 2.7×10^{-4}% and 1.9×10^{-4}%. The other signals exhibit much higher FAPs (>90%).

To check that the phase, amplitude, and frequency of the RV planet candidates are consistent, we used an apodized sine periodogram (ASP; Hara et al. 2022) consisting of fitting the coefficients A and B of an apodized sine function,

$$e^{-\frac{(t-t_0)^2}{2\tau^2}}(A\cos\omega t + B\sin\omega t), \quad (1)$$

for a grid of values of frequency, ω, signal lifetime, τ, and signal centre, t_0. We applied the ASP iteratively: the signal with the best fit is removed from the data, and then the ASP is computed on the residuals. We show the first three iterations in Fig. A.5, and find that Candidate#1 and Candidate#2 are consistent with being strictly periodic (i.e. the value of τ is compatible with $+\infty$). Overall, the GLS and ℓ_1 periodograms, correlation analyses, and signal consistency strongly suggest that the two planet candidates are fiducial planets, which we further study in Sect. 4.2.

[8] We used the `PyAstronomy` implementation (Czesla et al. 2019), which is available at https://github.com/sczesla/PyAstronomy

[9] In this periodogram, we forced the algorithm to explore signals above the Nyquist frequency to unveil possible hints of K2-157 b.

3. Stellar characterization

K2-157 is a late G-type star (V = 12.792 ± 0.057 mag, B-V = 0.805 mag; Henden et al. 2016) located in the solar neighbourhood (π = 3.446 ± 0.015 mas; Gaia Collaboration 2023). In Table 1, we compile its main astrometric and photometric properties from the literature. Mayo et al. (2018) used one spectrum acquired with the TRES spectrograph to derive the spectroscopic parameters $T_{\rm eff}$, log g, and [Fe/H] through the Stellar Parameter Classification (SPC) tool (Buchhave et al. 2012). The authors obtained $T_{\rm eff}$ = 5456 ± 50 K, [Fe/H] = 0.13 ± 0.08 dex, and log g = 4.55 ± 0.10, and input them into the `isochrones` package (Morton 2015) to derive a stellar mass and radius of $M_\star = 0.940^{+0.023}_{-0.027}$ M$_\odot$ and $R_\star = 0.876^{+0.045}_{-0.025}$ R$_\odot$, respectively. The photometry-based TESS Input Catalog (TIC v8.2; Stassun et al. 2018) obtains compatible values: $T_{\rm eff} = 5337^{+147}_{-159}$ K, log $g = 4.478^{+0.092}_{-0.069}$, $M_\star = 0.93^{+0.12}_{-0.10}$ M$_\odot$, and $R_\star = 0.921^{+0.043}_{-0.059}$ R$_\odot$. In the following sections, we describe our stellar characterisation based on a high-resolution, high-S/N ESPRESSO spectrum obtained from the co-adding of the 49 individual observations.

3.1. Stellar parameters and chemical abundances

We used the spectral analysis technique ARES+MOOG to derive the stellar atmospheric parameters ($T_{\rm eff}$, log g, micro-turbulence, and [Fe/H]), following the methodology described in Sousa et al. (2021); Sousa (2014); Santos et al. (2013). The latest version of ARES[10] (Sousa et al. 2007, 2015) was used to consistently measure the equivalent widths (EW) of a list of iron lines presented in Sousa et al. (2008). We used a minimisation process to find the ionisation and excitation equilibrium and converge to the best spectroscopic parameters. We used a grid of Kurucz model atmospheres (Kurucz 1993) and the radiative transfer code MOOG (Sneden 1973). The derived parameters are listed in Table 1. We also derived the trigonometric surface gravity using *Gaia* DR3 data following the methodology described in Sousa et al. (2021). The mass and radius of the star were inferred using PARAM 1.3[11] (da Silva et al. 2006): $M_\star = 0.890 \pm 0.029$ M$_\odot$ and $R_\star = 0.860 \pm 0.019$ R$_\odot$.

Chemical abundances are relevant to study the internal composition of highly irradiated rocky planets such as K2-157 b, since they are considered to be a good proxy of the original composition of the proto-planetary discs (e.g. Adibekyan et al. 2021). We derived the abundances of Mg and Si using the same tools and models as for stellar parameter determination, as well as the classical curve-of-growth analysis method, assuming local thermodynamic equilibrium (e.g. Adibekyan et al. 2012, 2015). Although the EWs of the spectral lines were automatically measured with ARES, for Mg, which has only three lines available, we performed a careful visual inspection of the EWs. We list the inferred abundances in Table 1.

3.2. Rotation period through the log($R'_{\rm HK}$) activity index

The log($R'_{\rm HK}$) values measured by the ESPRESSO DRS range from −5.214 ± 0.019 to −4.911 ± 0.015, indicating that K2-157 is a chromospherically inactive star (i.e. log $R'_{\rm HK} < -4.75$; Vaughan & Preston 1980; Middelkoop 1982; Henry et al. 1996; Gondoin 2020). We adopted a log($R'_{\rm HK}$) of −5.077 ± 0.049, which we obtained as the median value of the 49 individual

[10] Available at https://github.com/sousasag/ARES
[11] Available at http://stev.oapd.inaf.it/cgi-bin/param_1.3

Table 1. Stellar properties of K2-157 compiled from the literature and derived in this work (Sect. 3).

Parameter	Value	Reference
Identifiers		
K2	157	(1)
EPIC	201130233	(2)
TIC	349445372	(3)
UCAC4	422-055378	(4)
Gaia DR3	3596333042162818304	(5)
Astrometric properties		
RA, Dec	12:15:00.36, −5:46:55.27	(5)
μ_α (mas yr^{-1})	36.683 ± 0.017	(5)
μ_δ (mas yr^{-1})	−7.522 ± 0.012	(5)
Parallax (mas)	3.446 ± 0.015	(5)
RV (km s^{-1})	44.5 ± 1.4	(5)
Atmospheric parameters and spectral type		
$T_{\rm eff}$ (K)	5334 ± 64	(6)
log g (cgs)	4.45 ± 0.04	(6)
[Fe/H] (dex)	0.02 ± 0.04	(6)
$\xi_{\rm t}$ (km s^{-1})	0.73 ± 0.04	(6)
SpT	G9 V	(6)
Physical parameters		
$R_\star$ (R$_\odot$)	0.860 ± 0.019	(6)
$M_\star$ (M$_\odot$)	0.890 ± 0.029	(6)
Age (Ga)	8.8 ± 4.0	(6)
$v \sin i_\star$ (km s^{-1})	<3	(6)
log R'_{HK} (dex)	−5.077 ± 0.049	(6)
$P_{\rm rot,H_\alpha}$ (†) (d)	$36.76^{+0.40}_{-0.44}$	(6)
Chemical abundances		
[Mg/H] (dex)	0.07 ± 0.05	(6)
[Si/H] (dex)	0.05 ± 0.05	(6)
Photometric properties		
V (mag)	12.792 ± 0.057	(7)
B (mag)	13.597 ± 0.049	(7)
g' (mag)	13.160 ± 0.006	(7)
r' (mag)	12.579 ± 0.012	(7)
i' (mag)	12.387 ± 0.018	(7)
z' (mag)	12.367 ± 0.061	(7)
J (mag)	11.398 ± 0.022	(8)
H (mag)	11.023 ± 0.022	(8)
K$_s$ (mag)	10.980 ± 0.023	(8)
Galactic space velocities and membership		
$U_{\rm LSR}$ (††) (km s^{-1})	−66.89 ± 0.31	(6)
$V_{\rm LSR}$ (††) (km s^{-1})	5.15 ± 0.74	(6)
$W_{\rm LSR}$ (††) (km s^{-1})	45.65 ± 1.14	(6)
Gal. population (††)	Thin disc (54%)	(6)

Notes. (†) $P_{\rm rot,H_\alpha}$ was obtained by fitting a sinusoidal model to the H_α activity index ($\Delta\mathcal{Z}$ = +2.2; Sect. 4.3), and it is compatible with the $P_{\rm rot}$ estimated from empirical log($R'_{\rm HK}$)-$P_{\rm rot}$ relations (Sect. 3.2). (††) UVW are referred to the local standard of rest from Schönrich et al. (2010), and the probability is based on the prescription by Bensby et al. (2014). (1) Mayo et al. (2018); (2) Huber et al. (2016); (3) Stassun et al. (2018); (4) Zacharias et al. (2013); (5) Gaia Collaboration (2023); (6) This work; (7) Henden et al. (2016); (8) Skrutskie et al. (2006).

measurements. The error bar corresponds to the largest value between the median uncertainty (i.e. 0.0067) and the standard deviation of the measurements (i.e. 0.049). The $\log(R'_{\rm HK})$ index has been shown to correlate with the stellar rotation period through different age–rotation–activity relations, which also depend on the $B - V$ colour (Noyes et al. 1984; Mamajek & Hillenbrand 2008) or spectral type (Suárez Mascareño et al. 2016). The UCAC4 survey (Zacharias et al. 2013) measures B = 13.609 ± 0.010 mag and V = 12.823 ± 0.020 mag ($B - V$ = 0.786 ± 0.022) for K2-157. The APASS survey (Henden et al. 2016) DR10 (Henden 2019) measures B = 13.597 ± 0.049 mag and V = 12.792 ± 0.057 mag ($B - V$ = 0.805 ± 0.075 mag). The resulting $B - V$ colours of both surveys are compatible with a t-statistic of 0.09, so we selected the more precise value from UCAC4. We used the `pyrhk` code[12] to estimate the rotation period of K2-157 by following the relations from Noyes et al. (1984) and Mamajek & Hillenbrand (2008), and obtain $P_{\rm rot}$ = 42.6 ± 7.8 d and $P_{\rm rot}$ = 46.4 ± 4.2 d, respectively. From the latter, we also obtain an estimated age of 8.8 ± 4.0 Ga. We also used the updated relation for GKM stars from Suárez Mascareño et al. (2016), obtaining $P_{\rm rot}$ = 39.0 ± 3.5 d. Interestingly, these $P_{\rm rot}$ estimations are in quite good agreement with the prominent peak at ≃37 d found in the H_α indicator. In Sect. 4.3, we analyse in more detail the time series of the activity indicators to try to measure the true $P_{\rm rot}$.

4. Analysis and results

We aim to make a comprehensive characterisation of the K2-157 planetary system. Given the signal complexity shown in the RV periodograms and the large amount of data provided by K2 and TESS we split the analysis into different steps.

4.1. Model inference and parameter determination

We inferred the models that best describe our data sets and determined the associated parameters through Bayesian inference (Bayes & Price 1763). In brief, we first built Gaussian likelihood functions assuming that our data (D) is normally distributed, and then obtained both the posterior distributions of the parameters of the models (M_i) and the Bayesian evidences $\mathcal{Z}_i = P(D|M_i)$ through dynamic nested sampling (see Buchner et al. 2014; Higson et al. 2019, for a detailed description of the algorithm). Dynamic nested sampling has been proven to tackle high-dimensional problems better than traditional nestled sampling algorithms thanks to the inclusion of dynamically changing live-points, allowing more exhaustive explorations of the parameter space. We used the nested sampling implementation in `dynesty`[13] (Speagle 2020) and considered 5000 live-points with a conservative stopping criterion $\Delta\mathcal{Z} < 10^{-5}$, $\Delta\mathcal{Z}$ being the Bayesian evidence update during each iteration.

We searched for the best models describing our data through model comparison. To do so, we followed Occam's razor principle, so that we always selected the simplest possible model unless there was a more complex one with significantly larger evidence. Jeffreys (1961) empirically estimated that differences of the logarithmic evidences $\mathcal{B} = \ln(\mathcal{Z}_{\rm M_1}) - \ln(\mathcal{Z}_{\rm M_2})$ between 1 and 2.5 indicate weak evidence in favour of the higher evidence model, differences between 2.5 and 5 indicate a moderate evidence, while differences larger than 5 reflect strong evidence. We adopt this criterion and hence only consider that a complex model better describes our data than a simpler one if $\mathcal{B} > 5$.

4.2. Blind search for RV planetary signals

We followed the procedure described in Sect. 4.1 to search for planetary signals in the ESPRESSO data with no prior assumptions on their existence (i.e. blind search). We built a total of 21 models involving one, two, and three circular and eccentric orbits with and without long-term linear and quadratic trends.

We built the planetary models through Keplerians as implemented in the `radvel` package[14] (Fulton et al. 2018) by adopting the parametrization $P_{\rm orb}, T_0, K, \sqrt{e}\cos(\omega)$, and $\sqrt{e}\sin(\omega)$, where $P_{\rm orb}$ is the planetary orbital period, T_0 is the time of inferior conjunction, K is the semi-amplitude, e is the orbital eccentricity, and ω is the argument of the periastron of the orbit. Models with linear drifts, quadratic trends, or without long-term trends, were implemented as $\delta \times (t - t_{\rm init})^2 + \gamma \times (t - t_{\rm init}) + v_{\rm sys}$, where t is the Julian date and $t_{\rm init}$ corresponds to the first observing time ($t_{\rm init}$ = JD 2 458 533.735). We note that $v_{\rm sys}$ corresponds to the systemic velocity of the star as measured by ESPRESSO at $t = t_{\rm init}$. In addition, we incorporated a white noise component (i.e. a jitter term; $\sigma_{\rm jit}$) which we added quadratically to the formal RV uncertainties (σ_i): $(\sigma_i^2 + \sigma_{\rm jit}^2)^{0.5}$.

We considered wide and uninformative priors for all the parameters involved in the models to not biasing the search, parameter determination, and evidence computation. In particular, we adopted $\mathcal{U}(0, 400)$ d for $P_{\rm orb}$ (i.e. half the total ESPRESSO observing baseline), $\mathcal{U}(t_{\rm init}, t_{\rm init} + 400)$ d for T_0, $\mathcal{U}(0, 20)$ m s^{-1} for K, $\mathcal{U}(0, 10)$ m s^{-1} for $\sigma_{\rm jit}$, and $\mathcal{U}(-1, 1)$ for $\sqrt{e}\cos(\omega)$ and $\sqrt{e}\sin(\omega)$ in the eccentric cases. In Fig. 2, we show the log-evidences of each model subtracted from the lowest-evidence model (i.e. the zero-planet model with a quadratic trend), as in Lillo-Box et al. (2020). We label the models following the notation Xp [P_ic] [Y], where X is the total number of Keplerians, P_i indicates which planets are considered to have a circular orbit, and Y indicates whether the model has a linear (L) or quadratic (Q) trend. We find that the Bayesian evidence is boosted for the two-planet model with circular orbits and a quadratic trend, 2p1c2cQ. This model has the largest evidence, and meets the criterion for strong evidence ($\mathcal{B} > 5$) when compared to simpler models, thus positioning itself as the best description of the ESPRESSO RVs. The considerable evidence difference between this model and the other two-planet models highlights the importance of the quadratic trend, which exhibits a long-term high amplitude comparable to the Keplerians.

The analyses presented above indicate that the ESPRESSO RVs of K2-157 are best described when including two planetary signals, which coincide with the periodicities of Candidate#1 and Candidate#2 (Sect. 2.3 and Fig. 1). The ESPRESSO activity indicators show no hints of sinusoidal signals at these periodicities (Sect. 2.3 and Fig. A.2), strongly supporting a planetary origin. We note, however, that before considering these RV planetary signals as confirmed planets, we conducted more dedicated analyses of the stellar activity of K2-157 (Sect. 4.3), which definitively allowed us to refer to them as K2-157 c ($P_{\rm orb}$ = 25.97 d) and K2-157 d ($P_{\rm orb}$ = 66.58 d). In Table B.4, we show the median and 1σ (i.e. 68.3% credible intervals) of the posterior distributions of the fitted parameters of the 2p1c2cQ model. In Fig. 3, we plot the RV ESPRESSO data set together with the model evaluated on the median parameters. In Fig. C.1, we show a corner plot with the posterior distributions of the parameters.

[12] Available at https://github.com/gomesdasilva/pyrhk
[13] Available at https://github.com/joshspeagle/dynesty
[14] Available at https://radvel.readthedocs.io/en/latest

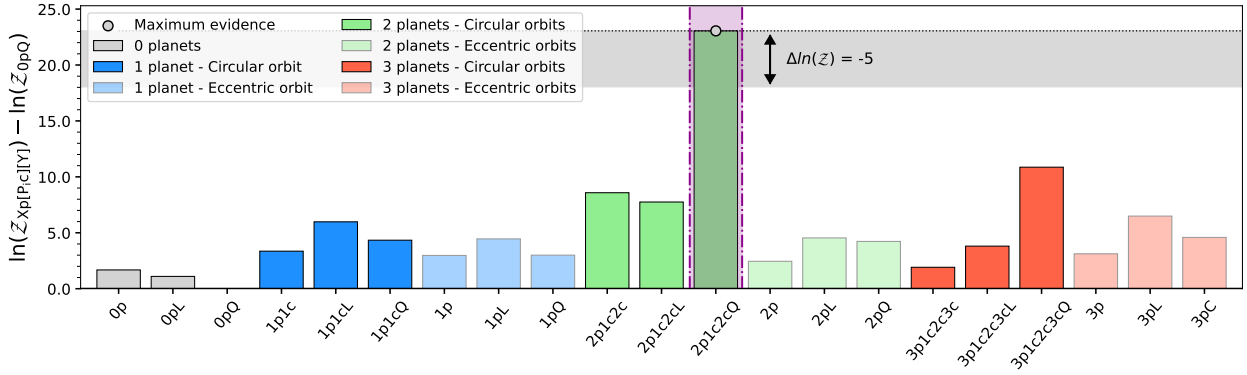


Fig. 2. Bar chart showing the differences of the log-evidences of the 21 tested models, which are labelled on the X axis. The grey, blue, green, and red bars represent models with zero, one, two, and three planets, respectively. The vertical magenta shade highlights the simplest model that best represents our data set (2p1c2cQ). The horizontal grey shade indicates the $0 \geq \Delta\ln(\mathcal{Z}) \geq -6$ region from the model with the largest evidence.

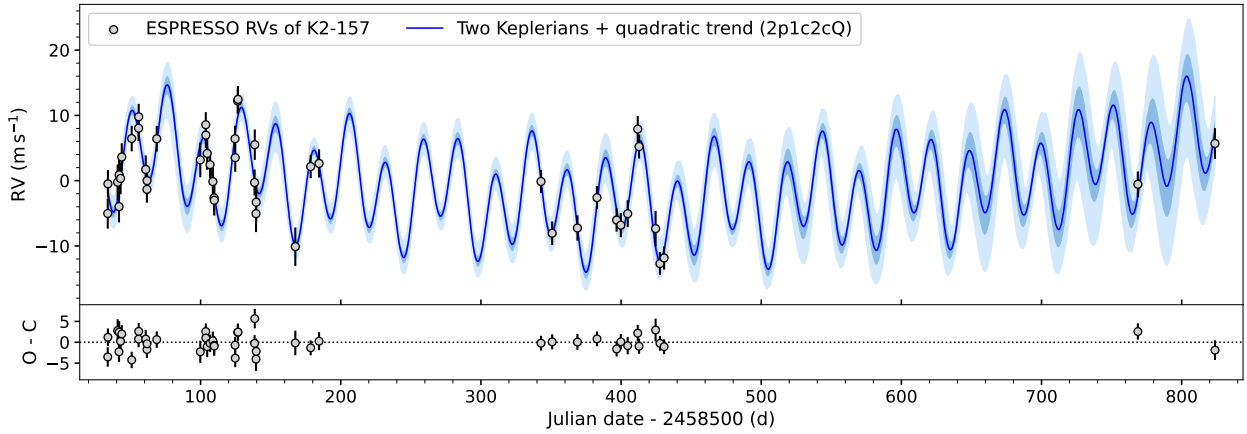


Fig. 3. RVs of K2-157. The solid blue line indicates the median posterior model that best represents our data set (i.e. two circular Keplerians plus a quadratic trend), and the dark and light blue shades correspond to the 1σ and 3σ confidence intervals, respectively.

In addition to the detection of two additional planet signals, we can draw two main conclusions from the blind-search analysis. First, the significant quadratic long-term trend suggests the existence of an additional long-period massive companion in the system, or, alternatively, the imprint of the magnetic cycle of the star (we can confidently discard an instrumental origin given the well-known ESPRESSO long-term stability). Lovis et al. (2011) found that long-term RV trends caused by the stellar magnetic cycle would be similarly detected in the FWHM indicator, and the opposite trend would be detected in the Contrast indicator. For K2-157, the FWHM shows a tentative upward trend, and the Contrast shows a clear linear downward trend with no hints of a parabolic behaviour. Hence, we cannot infer a preferred origin for the RV trend based on the indicators. The second conclusion is that the RV signal of K2-157 b is not detected in ESPRESSO data when considering wide, uninformative priors (i.e. through blind search). However, a tentative peak (FAP < 10%) with the exact periodicity of K2-157 b appears in the periodogram of the residuals of the two-planet model (Fig. 4, upper panel). This periodogram resembles the periodogram of the RVs after subtracting a quadratic trend plus the two most significant sinusoidal signals (Fig. 1, lower panel), hinting again that the RV signature of K2-157 b is embedded in our data.

4.3. Stellar activity and rotation period

The low $\log(R'_{\rm HK})$ activity index (i.e. –5.077 ± 0.049; Sect. 3.2) together with the absence of significant sinusoidal activity signals (Sect. 2.3) indicates that K2-157 is chromospherically inactive. While apparently challenging, the main goal of this section is to try to measure the rotation period of K2-157 by further exploring its activity indexes through a specific activity model.

Given that activity signals are not necessarily periodic (e.g. Ioannidis & Schmitt 2016) or sinusoidal (e.g. Dumusque et al. 2014), we modelled the activity indicators with a Gaussian Process regression (GP; Rasmussen & Williams 2006; Roberts et al. 2012) defined by a quasiperiodic kernel (Ambikasaran et al. 2015). This GP is physically motivated (i.e. it depends on a set of hyperparameters interpretable through different spot/plage properties) and can be implemented through `george`[15] as:

$$K_{QP}(\tau) = \eta_1^2 \exp\left[-\frac{\tau^2}{2\eta_2^2} - \frac{2\sin^2\left(\frac{\pi\tau}{\eta_3}\right)}{\eta_4^2}\right]. \quad (2)$$

The hyperparameter η_1 scales with the amplitude of the stellar activity signal. η_3 corresponds to the main periodicity of the signal, and it is considered to reflect the stellar rotation period (i.e. $\eta_3 = P_{\rm rot}$; Angus et al. 2018). η_2 is the length-scale of exponential decay, and thus it is considered a measure of the timescale of growth and decline of the active regions. η_4 controls the relative

[15] Available at https://github.com/dfm/george

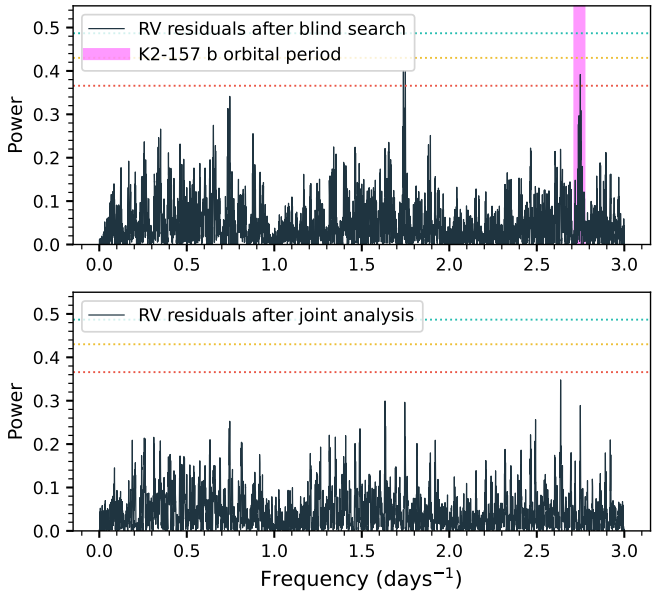


Fig. 4. GLS periodogram of the residual RVs after subtracting the two-planet model from the blind-search analysis (Sect. 4.2) and the three-planet model from the joint analysis (Sect. 4.4). The horizontal dashed red, orange, and green lines indicate the 10, 1.0, and 0.1% FAP levels, respectively.

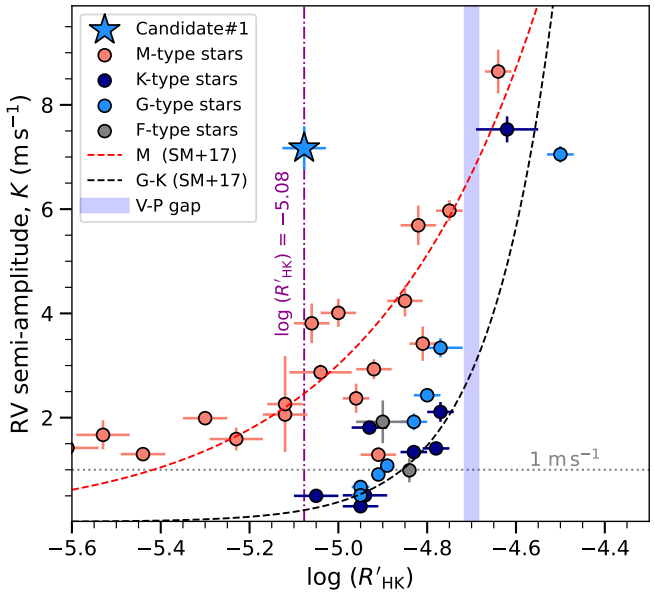


Fig. 5. RV semi-amplitude (K) of rotation-induced signals versus the chromospheric activity level log(R'_{HK}) of 37 stars studied in Suárez Mascareño et al. 2017 (SM+17). The blue star corresponds to the semi-amplitude of Candidate#1. The vertical band represents the Vaughan-Preston (V-P) gap (Vaughan & Preston 1980) separating inactive and active stars at log(R'_{HK}) ≃ −4.7.

importance between the long-term decay and the periodic variability (see Haywood et al. 2014; Faria et al. 2016; Angus et al. 2018, for detailed descriptions of these parameters).

Similarly to the blind-search RV analysis, we followed the procedure described in Sect. 4.1 to search for activity signals in the ESPRESSO indicators with no prior assumptions on their existence: $\eta_1 \in \mathcal{U}(0{,}1000)$, $\eta_3 \in \mathcal{U}(0{,}100)$, $\eta_2 \in \mathcal{LU}(0.001{,}1000)$, and $\eta_4 \in \mathcal{LU}(0.001{,}100)$. In Fig. A.6, we show the posterior distributions of the η_3 (or $P_{\rm rot}$) hyperparameter for each time series. η_1 either converged to a non-zero amplitude or showed a well-constrained zero-truncated distribution, and both η_2 and η_4 always showed unconstrained posterior distributions. The η_3 distribution converged at $\eta_{3,{\rm H}_\alpha} = 37.03^{+1.25}_{-0.92}$ d for the H_α time series, where we had previously identified a prominent GLS peak at 36.9 d (Sect. 2.3). In contrast, the other five indicators show unconstrained η_3 distributions. We note, however, over-density regions of compatible solutions at $\eta_3 \simeq 37$–38 d in the Na indicator, and at $\eta_3 \simeq 35$–36 d in the FWHM indicator, which could be reflecting the same activity signal. Interestingly, this periodicity falls within the 1σ confidence interval of the expected $P_{\rm rot}$ from the log(R'_{HK})-$P_{\rm rot}$ empirical relations from Suárez Mascareño et al. 2016 (Sect. 3.2), which further supports a stellar origin for the signal. We note that the log-evidences do not favour the activity model against the null hypothesis, with $\Delta\mathcal{Z}$ ranging from −11 to −2. Getting negative evidence indicates that the considered activity model is too complex for the studied data sets. In particular, for the case of the H_α indicator, where only η_1 and η_3 converged, the unconstrained η_2 and η_4 hyperparameters are useless and so can be safely discarded.

We repeated the analysis by considering a simple sinusoid plus a linear trend as the activity model. The log-evidence of this model compared to the linear trend alone is $\Delta\mathcal{Z} = +2.2$, and its periodicity converges at $P_{{\rm rot},{\rm H}_\alpha} = 36.76^{+0.40}_{-0.44}$ d (i.e. compatible with $\eta_{3,{\rm H}_\alpha}$ within 1σ). We note that this log-evidence is not high enough to claim this $P_{\rm rot}$ as statistically significant, but being positive and near the moderate evidence threshold (i.e. $\Delta\mathcal{Z} > 2.5$) we consider it as a good candidate to be the true $P_{\rm rot}$, especially when also taking into account that it matches the empirical predictions obtained from the log(R'_{HK}) index. We thus report this value in Table 1 while including a cautionary footnote highlighting its still not significant Bayesian Evidence. In Fig. A.7 (left panel), we show the complete H_α time series together with the median posterior model. In the right panel, we show the H_α data folded to the inferred $P_{{\rm rot},{\rm H}_\alpha}$.

We also tested the activity-unrelated nature of Candidate#1 by taking into account its large RV amplitude (i.e. $K_{\#1} = 7.10 \pm 0.49$ m s^{-1}). Suárez Mascareño et al. 2017 (SM+17) used HARPS RVs of 37 stars to find that the log(R'_{HK}) index and the rotation-induced RV semi-amplitude are correlated. In Fig. 5, we contextualise Candidate#1 within their sample and empirical relations. A GK star with a log(R'_{HK}) of −5.08 is expected to generate a RV semi-amplitude of about 0.2 m s^{-1}, which is well below the observed 7 m s^{-1} for Candidate#1. We note that this prediction comes from an extrapolation, given that SM+17 relations do not contain stars with such a low log(R'_{HK}), so the exact value should be taken with care. Still, stars with log(R'_{HK}) $\lessapprox -4.9$ show semi-amplitudes $\lessapprox 1$ m s^{-1}, which are still well below the observed signal semi-amplitude.

From the analyses presented above, we can safely claim that Candidate#1 is not generated by the stellar rotation of the star, and instead, $P_{{\rm rot},{\rm H}_\alpha} = 36.76^{+0.40}_{-0.44}$ d positions as the most likely rotation period of K2-157. This, together with the blind-search analysis, allows us to confirm the planetary nature of Candidate#1 ($P_{\rm orb} = 25.97$ d) and Candidate#2 ($P_{\rm orb} = 66.62$ d), which we refer to as K2-157 c and K2-157 d, respectively.

4.4. Joint RV and transit analysis

We inferred the final parameters of the K2-157 system by jointly modelling the ESPRESSO RVs and K2 photometry through a joint RV (3p1c2c3cQ) and transit model.

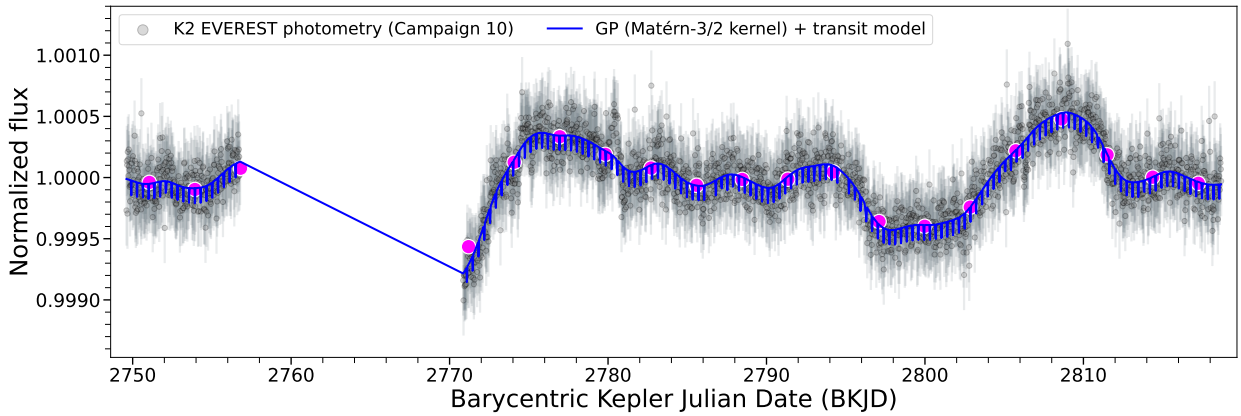


Fig. 6. K2 EVEREST photometry of K2-157 (Campaign 10) together with the median posterior model (transit + GP) inferred in Sect. 4.4. The magenta data points correspond to bins of 3 d. BKJD equals Barycentric Julian Date (BJD) − 2 454 833 d.

We used the quadratic limb-darkened transit model from Mandel & Agol (2002) as implemented in `batman`[16] (Kreidberg 2015). This model is defined by seven parameters: the orbital period of the transiting planet ($P_{\rm orb}$), its time of inferior conjunction (or time of mid-transit, T_0), the inclination of the planetary orbit (i), the planet-to-star radius ratio ($R_{\rm p}/R_\star$), the quadratic limb darkening (LD) coefficients u_1 and u_2, and the semimajor axis scaled to the stellar radius ($a/R_\star$). We parametrized the LD parameters through the prescription for effective uninformative sampling proposed by Kipping (2013): $q_1 = (u_1 + u_2)^2$, and $q_2 = 0.5\, u_1\, (u_1 + u_2)^{-1}$, and also parametrized $a/R_\star$ through the stellar mass ($M_\star$) and radius ($R_\star$) in order to better constrain the model parameters (Sozzetti et al. 2007).

As we can see in Fig. 6, K2 data is affected by considerable correlated noise provoking low-frequency trends, which is a well-known behaviour caused by the spacecraft drift (potentially mixed with some degree of stellar variability). In order to better preserve the shape and depth of the transits, we modelled jointly the transit signal and correlated noise through a GP. This procedure has been proven successful to model shallow transit signals (e.g. Dransfield et al. 2022; Damasso et al. 2023) and ensures a proper propagation of the uncertainties of the model parameters (e.g. Leleu et al. 2021). We chose a GP defined by a Matérn-3/2 kernel, which, given its flexibility, is one of the preferred kernels to model photometric satellite data with an unknown mixture of instrumental and stellar noise (e.g. Kossakowski et al. 2021; González-Álvarez et al. 2022; Murgas et al. 2023; Morello et al. 2023; Lacedelli et al. 2024). This kernel can be written as:

$$k(x_i, x_j) = \eta_\sigma^2 \left[\left(1 + \frac{1}{\epsilon}\right) e^{-(1-\epsilon)\,\sqrt{3}\tau/\eta_\rho} \cdot \left(1 - \frac{1}{\epsilon}\right) e^{-(1+\epsilon)\,\sqrt{3}\tau/\eta_\rho} \right], \quad (3)$$

where $\tau = x_i - x_j$ is the temporal separation between two time stamps, and η_σ and η_ρ are two hyperparameters that represent the characteristic amplitude and timescale of the correlated variations, respectively. The parameter ϵ controls the approximation to the exact kernel, which we fixed to its default value of 10^{-2} (Foreman-Mackey et al. 2017).

We ran the joint fit analysis through the procedure described in Sect. 4.1 and using the priors specified in Table B.5. Most priors are uniform (either uninformed or poorly informed), except the stellar mass and radius, for which we used Gaussian priors based on the characterisation described in Sect. 3. For the quadratic LD coefficients, we tested unconstrained uniform priors, and also constrained Gaussian priors based on the `ldtk` package[17] (Parviainen & Aigrain 2015). This package uses the spectroscopic atmospheric parameters $T_{\rm eff}$, log g, and [Fe/H], together with the instrumental transmission curve (*Kepler* in this case) to infer the coefficients of any LD law (quadratic in this case) based on the synthetic spectra library from Husser et al. (2013). We obtain $u_1 = 0.5672 \pm 0.0015$ and $u_2 = 0.1154 \pm 0.0022$ (i.e. $q_1 = 0.4660 \pm 0.0037$ and $q_2 = 0.4154 \pm 0.0014$). We note that the uncertainties of theoretical LD coefficients have been commonly found to be misestimated (e.g. Patel & Espinoza 2022), which can induce biases in the transit modelling. To try to avoid this situation, we performed three different modellings: considering the formal `ldtk` uncertainties, arbitrarily and conservatively enlarging them up to 0.3, and uniformly sampling the parameter space with $\mathcal{U}(0, 1)$ priors. We find that in the unconstrained case, the posterior q_1 and q_2 distributions remain quite unconstrained, and that in the more constrained scenarios, the resulting planetary parameters are compatible with the unconstrained case at the 1σ level. Therefore, we can conclude that the a priori constraining level of the LD coefficients does not have an impact on the characterisation of this system, and we thus arbitrarily chose to report the unconstrained case. In Table B.5, we show the median and 1σ intervals of the posterior parameter distributions.

We draw three con clusions from the results of the joint analysis. First, the RV semi-amplitudes of planets K2-157 c and K2-157 d are compatible at 1σ with those inferred from the blind-search analysis. Second, our derived orbital and physical parameters for K2-157 b are also compatible with those from previous K2-based works. In particular, the planet-to-star radius ratio ($R_{\rm p,b}/R_\star = 0.00996 \pm 0.00094$) agrees with that of Mayo et al. 2018 ($R_{\rm p,b}/R_\star = 0.0111^{+0.0014}_{-0.0010}$) with a t-statistic of 0.83 and with that of Adams et al. 2021 ($R_{\rm p,b}/R_\star = 0.0107^{+0.0011}_{-0.0006}$) with a t-statistic of 0.66. The third conclusion is that we were able to measure the RV semi-amplitude of K2-157 b at a $\simeq 2.7\sigma$ level, $K_{\rm b} = 1.10^{+0.39}_{-0.41}$ m s^{-1}, which translates into a mass of $M_{\rm p,b} = 1.14^{+0.41}_{-0.42}$ M$_\oplus$ (< 2.4 M$_\oplus$ at 3σ)[18].

[16] Available at https://github.com/lkreidberg/batman

[17] Available at https://github.com/hpparvi/ldtk

[18] We note that some authors opt to report the 3σ mass upper limit when the semi-amplitude significance is below 3σ (e.g. Bonomo et al. 2023; Osborn et al. 2023; Luque et al. 2023; Cointepas et al. 2024), while others prefer to report the median and 1σ confidence intervals for significances about $\simeq$2–3σ (e.g. Weiss et al. 2013; Barros et al. 2022; Peterson et al. 2023; Polanski et al. 2024). For K2-157 b, given the closeness to the 3σ threshold, we decide to report both the 1σ uncertainties and the upper limit (in brackets).

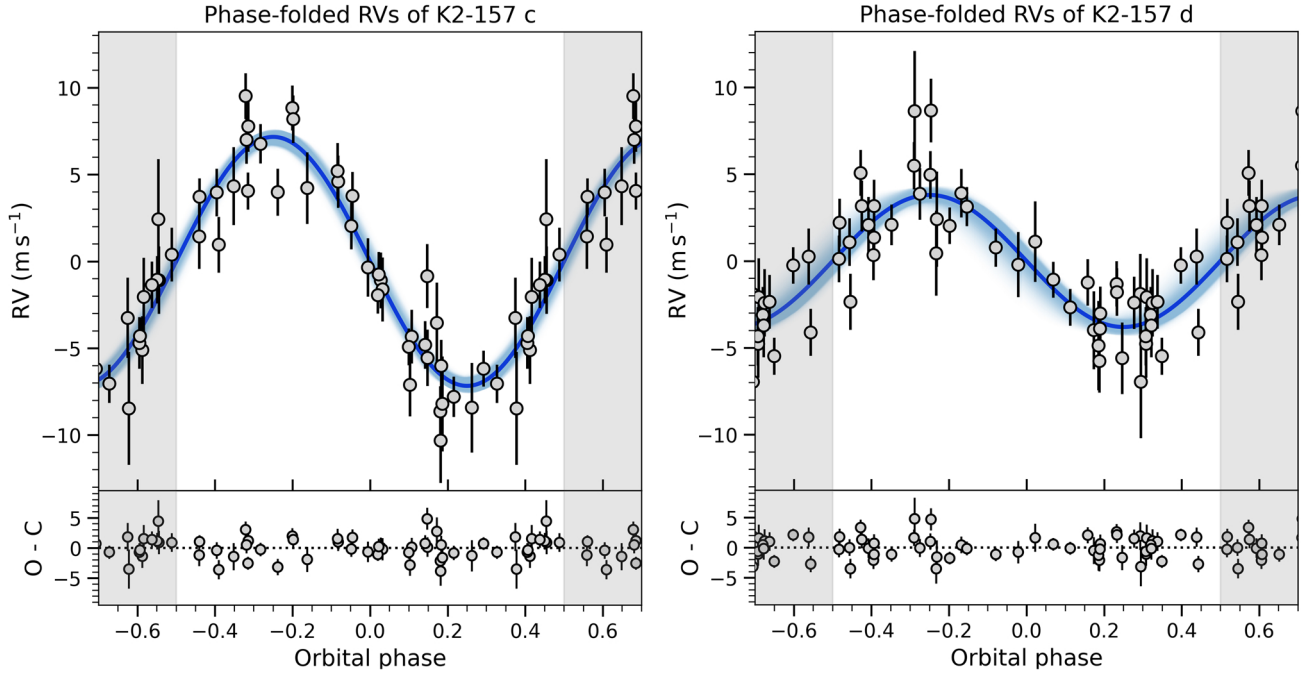


Fig. 7. ESPRESSO RVs of K2-157 c (left) and K2-157 d (right) folded to their respective orbital periods inferred in Sect. 4.4. The solid blue lines indicate the median posterior models, and the shades indicate the 1σ confidence intervals.

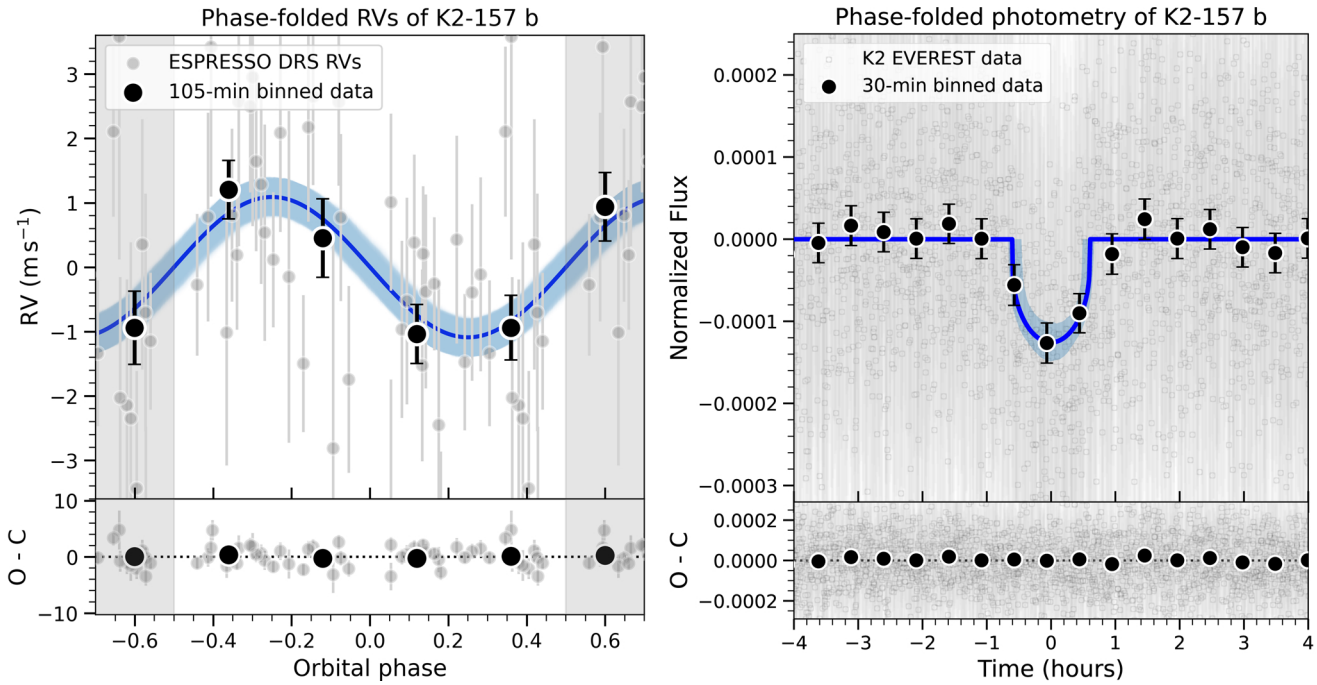


Fig. 8. ESPRESSO RVs (left) and K2 photometry (right) of K2-157 b folded to its orbital period inferred in Sect. 4.4. In both panels, the solid blue line indicates the median posterior model, and the shade indicates the 1σ confidence interval.

In Fig. 7, we show the ESPRESSO RVs caused by K2-157 c and K2-157 d subtracted from the other components in the model and folded to their inferred orbital periods. In Fig. 6, we show the C10 K2 light curve together with the transit + GP model for K2-157 b. In Fig. 8, we show the ESPRESSO RVs and K2 photometry folded to the orbital period of K2-157 b. In Fig. 4, we show the periodogram of the RV residuals. In Fig. C.2, we show a corner plot with the posterior distributions of the fit parameters.

Finally, while not preferred by the RV data (Sect. 4.2), we performed an additional joint analysis by letting the orbital eccentricities vary uniformly between 0 and 1 to infer the upper limits compatible with our data set. As a result, the posterior of e_b resulted in a quasi-flat, unconstrained distribution. However, from the posteriors of e_c and e_d, truncated at zero, we were able to derive 3σ upper limits of $e_c < 0.2$ and $e_d < 0.5$. Regarding the remaining parameters, we find values compatible at 1σ with those from the circular model. These eccentricities

are poorly constrained, but still allow us to discard highly eccentric orbits for K2-157 c and K2-157 d. In Sect. 5.3, we conduct an orbital stability analysis of the system to try to better constrain the eccentricities of these planets.

4.5. Possible transits and inclinations of K2-157 c and d

We explored the possibility that K2-157 c and K2-157 d transit their host star and studied the range of orbital inclinations compatible with the K2 data. To do so, we first considered the measured minimum masses and used the empirical mass-radius relations from Chen & Kipping (2017) to estimate the minimum radii for both planets, $R_{\rm p,c} = 6.03^{+2.48}_{-1.78}$ R$_\oplus$ and $R_{\rm p,d} = 5.21^{+1.94}_{-1.56}$ R$_\oplus$, which correspond to minimum transit depths of $\delta_{\rm c} = 4.1 \pm 2.4$ ppt and $\delta_{\rm d} = 3.1 \pm 1.9$ ppt. These transit signals would have been clearly detected both within K2 and TESS data (see Sects. 2.1 and 2.2). The non-detections can be explained through three possible scenarios: (1) the planets transit but the transit times do not fall within the photometric temporal baseline, (2) the planets transit with a grazing configuration that reduces the observed transit depth, or (3) the planets do not transit at all. We tested scenario 1 by propagating the RV-derived ephemeris to the K2 and TESS observing windows. In Fig. A.9, we show the expected transit locations with their associated 1σ uncertainties. We see that at least one transit of K2-157 c would have been observed in the K2 data. In contrast, the larger periodicity and ephemeris uncertainty of K2-157 d prevent us from determining whether it would have been observed to transit within this data set. We tested scenarios 2 and 3 for K2-157 c by repeating the joint fit from Sect. 4.4 but including a transit component for this planet[19]. We set a uniform prior for the orbital inclination $\mathcal{U}_{\rm c}(0,90)$ and a Gaussian prior for the minimum mass, which we translated into $R_{\rm p}/R_\star$ through the sampled inclinations and the mass-radius relation. We highlight that this approach accounts for the uncertainties in our mass determination and the scatter in the empirical relations, and it also considers the dependency of the true mass on the orbital inclination. The posterior distribution results in a 3σ upper limit of $i_{\rm c} < 88.4°$, which translates into a 3σ lower limit for the impact parameter of $b_{\rm c} > 1.15$. We note that this value corresponds to a configuration where the planet is outside the sky-projected stellar disc, and, in order to transit, it requires a planetary radius of at least $\simeq$14 R$_\oplus$, coinciding with the 3σ upper limit of the minimum radius estimated for K2-157 c.

4.6. Sensitivity limits and constraints on additional planets

We computed the sensitivity limits of the ESPRESSO data by following the procedure described in Standing et al. (2022) as used in previous works (Sairam & Triaud 2022; Grieves et al. 2022; Standing et al. 2023; Baycroft et al. 2023; John et al. 2023; Sairam et al. 2024; Balsalobre-Ruza et al. 2025). We began by running `kima`[20] (Faria et al. 2018) on the ESPRESSO RVs after removing the signals of K2-157 b, K2-157 c, and K2-157 d. `kima` utilises a diffusive nested sampling algorithm (Brewer et al. 2011) and allows the number of planetary signals (N_p) to be fit as a free parameter. This initial run ensures that there are no remaining signals in the residual data set.

We ran `kima` again with the number of planetary signals fixed to one. The posterior samples obtained from this run are compatible with the data, but their signals are not formally detected. For our analysis, we obtained over 520 000 samples. The 3σ upper limit is then calculated in period bins, yielding the detection limit, which can be seen as the blue line in Fig. 9. The uncertainty on this limit is calculated as described in Standing et al. (2023). Any planetary signal above the blue detection limit would have been detected in the blind search on the ESPRESSO data. This was the case for planets K2-157 c and K2-157 d, which are well above the detection limit in Fig. 9. The signal expected from K2-157 b is below the detection limit, which explains why the blind search was unable to detect it. Overall, from Fig. 9 we conclude that we can discard the presence of planets with $M_{\rm p} \gtrsim 2$ M$_\oplus$ and $P_{\rm orb} \lesssim 1$ d, $M_{\rm p} \gtrsim 4$ M$_\oplus$ and $P_{\rm orb} \lesssim 10$ d, and $M_{\rm p} \gtrsim 10$ M$_\oplus$ and $P_{\rm orb} \lesssim 200$ d.

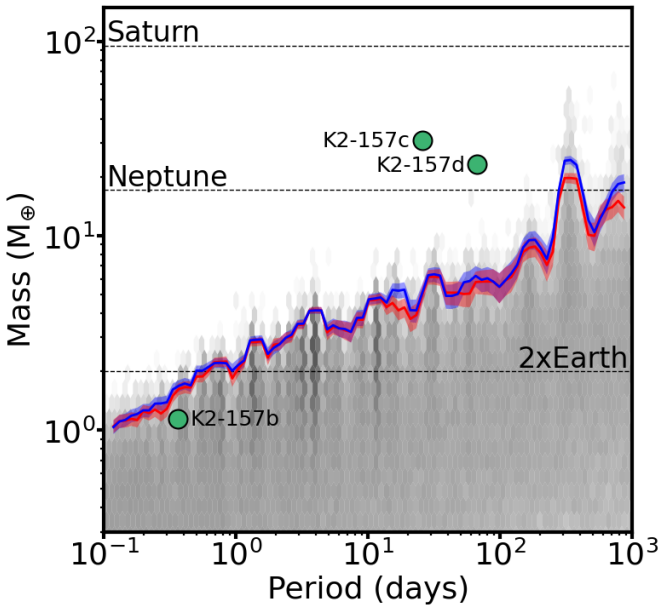


Fig. 9. Hexbin plot of posterior samples obtained from `kima` runs on the residual RV data with N_p fixed to 1. The blue line shows the 3σ detection limit, whereas the red line shows the same limit computed on a subset of posterior samples with eccentricity <0.1. The uncertainties on these lines are illustrated by the faded lines of the associated colour.

5. Discussion

The mass determination ($M_{\rm p,b} = 1.14^{+0.41}_{-0.42}$ M$_\oplus$; < 2.4 M$_\oplus$ at 3σ) and subsequent RV confirmation of the USP Earth-sized planet K2-157 b ($P_{\rm orb,b} \simeq 8.8$ h; $R_{\rm p,b} = 0.935 \pm 0.090$ R$_\oplus$), together with the detection of two additional warm super-Neptune-mass planets, can provide insightful clues into the formation and evolution of this planetary system. USP planets such as K2-157 b are scarce in exoplanet catalogues, and those with relatively massive and warm companions are even rarer, which positions K2-157 as a relevant USP-hosting system to test planet formation and evolution theories. In Sect. 5.1, we contextualise and discuss the main properties of K2-157 b in the known population of USP planets (i.e. within the period-radius and mass-radius parameter spaces), and explore the recently identified dependency between the semi-major axis of USP planets and stellar spectral type. In Sect. 5.2, we contextualise K2-157 c and K2-157 d in the period-mass diagram of known neighbours of USP planets and discuss their unusual location in this region of the parameter space. In Sect. 5.4, we compare the properties

[19] We did not use TESS data for this analysis, given the much lower constraining capacity than K2's.
[20] Available at https://github.com/kima-org/kima

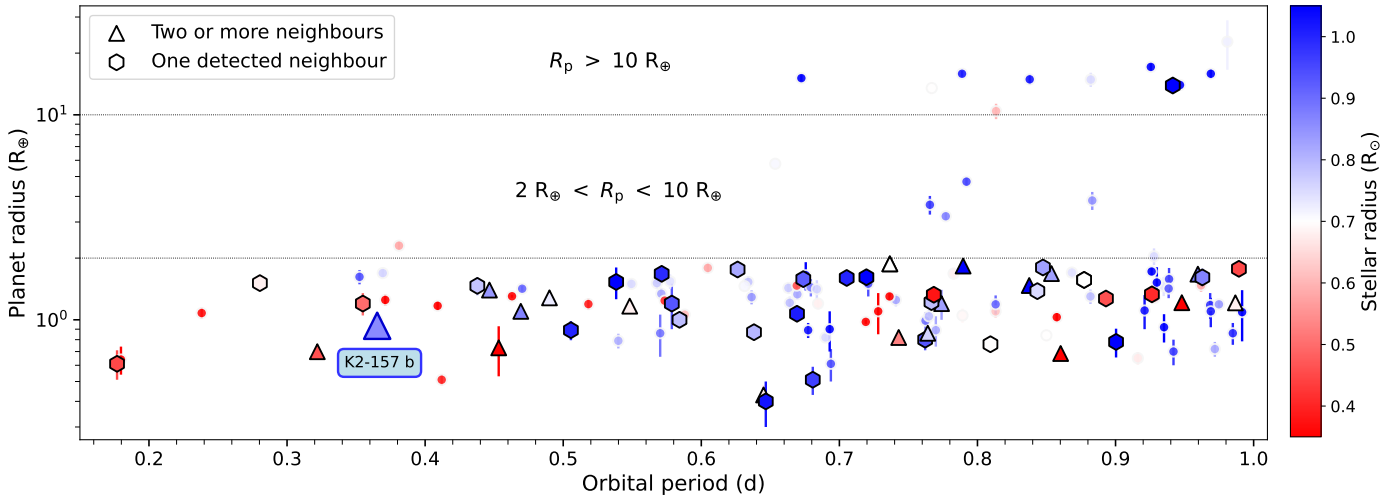


Fig. 10. Period-radius diagram of all known USP planets with radii constrained to a precision better than 30% (source: NASA Exoplanet Archive, accessed on 24/03/2025). The colour code indicates the radii of the stellar hosts, with the blueish and reddish tones indicating radii above and below $R_\star \simeq 0.7$ R$_\odot$, respectively. USP planets with one detected neighbour are highlighted with hexagonal symbols, while those with two or more neighbours are shown with triangular symbols.

of K2-157 to different formation and evolution theories of USP planets.

5.1. K2-157 b in context

5.1.1. Period-radius diagram

In Fig. 10, we show the period-radius diagram of USP planets with radii constrained to precisions better than 30%. Among the 135 planets composing the sample, 87% (i.e. 117 planets) show radii lower than 2 R$_\oplus$, while the remaining 13% (i.e. 18 planets) show a wide range of larger radii (i.e. 2 R$_\oplus$ < R_p < 23 R$_\oplus$). Interestingly, terrestrial USP planets (R_p < 2 R$_\oplus$) have been detected with orbital periods as short as 0.18 d (4.3 h; Rappaport et al. 2013; Smith et al. 2018), while larger USP planets have been only found with periods as short as 0.65 d (15.6 h; Morton et al. 2016; Wong et al. 2021). In this context, having an orbital period of 0.365 d (8.8 h), K2-157 b is the ninth shortest-period transiting planet known to date[21], only after KOI-1843.03 (Rappaport et al. 2013), K2-137 b (Smith et al. 2018), TOI-6255 b (Dai et al. 2024), K2-141 b (Barragán et al. 2018; Malavolta et al. 2018), GJ 367 b (Lam et al. 2021), TOI-2260 b (Giacalone et al. 2022), EPIC 206042996 c (Adams et al. 2021), and Kepler-78 b (Sanchis-Ojeda et al. 2013). Among these nine planets, four have been previously found to have additional planetary companions (Morton et al. 2016; Malavolta et al. 2018; Heller et al. 2019; Bonomo et al. 2023; Goffo et al. 2023). The discovery of K2-157 c and K2-157 d thus implies that more than half the shortest-period planets (five out of nine) have neighbours. Among these systems, only GJ 367 b is known to have more than one neighbour (Goffo et al. 2023), so K2-157 b becomes the second shortest-period planet known to have at least two neighbours. In the terrestrial region (R_p < 2 R$_\oplus$), 40% of USP planets (41% accounting for K2-157 b) have neighbours, while only 6% (i.e. WASP-18 c; Pearson 2019) of larger planets (R_p > 2 R$_\oplus$) are known to have neighbours[22]. Therefore, from a simple inspection of Fig. 10, we can infer the existence of at least two classes of USP planets with a well-defined division line at $R_\mathrm{p} \simeq 2$ R$_\oplus$. In addition to the different occurrence rates, orbital distribution, and fraction of systems with neighbours, small USP planets are known to be hosted by solar-metallicity stars, while hot Neptunes and hot Jupiters prefer higher metallicity hosts (see Dai et al. 2021, for a comparative study of USP planets). Given these differences, which suggest well-differentiated formation or evolution pathways, we focus our discussion on USP planets with R_p < 2 R$_\oplus$ (i.e. the population to which K2-157 b belongs).

The ultra-short orbital period of K2-157 b may place it near the Roche limit; that is, the star-planet separation where tidal forces exerted by the star are stronger than the planet's gravity. Below this threshold, a planet will start to disintegrate if the material strength is negligible. Following Rappaport et al. (2013), we estimated the orbital period of the Roche limit to be[23]

$$P_\mathrm{Roche} \approx 12.6\,\mathrm{h}\left(\frac{\rho_\mathrm{p}}{1\,\mathrm{g\,cm^{-3}}}\right)^{-\frac{1}{2}}. \quad (4)$$

We obtain P_Roche = 4.5 ± 1.1 h, so that the orbital period of K2-157 b is approximately twice that of the tidal disruption limit, $P_\mathrm{orb}/P_\mathrm{Roche}$ = 1.93 ± 0.45. Interestingly, the tidal love theory (Love 1892) predicts that rocky planets with $P_\mathrm{orb}/P_\mathrm{Roche} \simeq 2$ such as K2-157 b may undergo a certain degree of tidal distortion, with a long axis of about ≃2% longer than its short axis (see Lambeck 1980; Correia 2014; Dai et al. 2024), which would decrease its bulk density by ≃6% (e.g. Yoder 1995; Correia 2014). We applied Eq. (4) to the sample of known USP rocky planets with measured masses and radii, and find that K2-157 b has one of the lowest $P_\mathrm{orb}/P_\mathrm{Roche}$ ratios, making it an excellent

[21] In Fig. 10, K2-157 b appears to be the eighth shortest-period planet since EPIC 206042996 c and Kepler-78 b are perfectly overlaid with orbital periods of 0.355 d and radii of 1.20 R$_\oplus$.

[22] In addition, WASP-18 c is flagged as a 'controversial' planet in the NASA Exoplanet Archive (Akeson et al. 2013; Christiansen 2022).

[23] This equation is only valid for bodies in circular orbits composed of incompressible fluids with negligible bulk tensile strength. However, it serves as a good approximation for planets composed of iron and silicates since they are not highly compressible. According to Lai et al. (1993) and Rappaport et al. (2013), an extra multiplicative factor $(\rho_{0,\mathrm{p}}/\rho_\mathrm{p})^{-0.16}$ should be included in the expression to account for this effect. $\rho_{0,\mathrm{p}}$ is the central density of the planet and cannot be easily inferred, but the $(\rho_{0,\mathrm{p}}/\rho_\mathrm{p})^{-0.16}$ factor is only expected to vary from ≃0.85 to 1 for rocky planets (Rappaport et al. 2013), so we can neglect it.

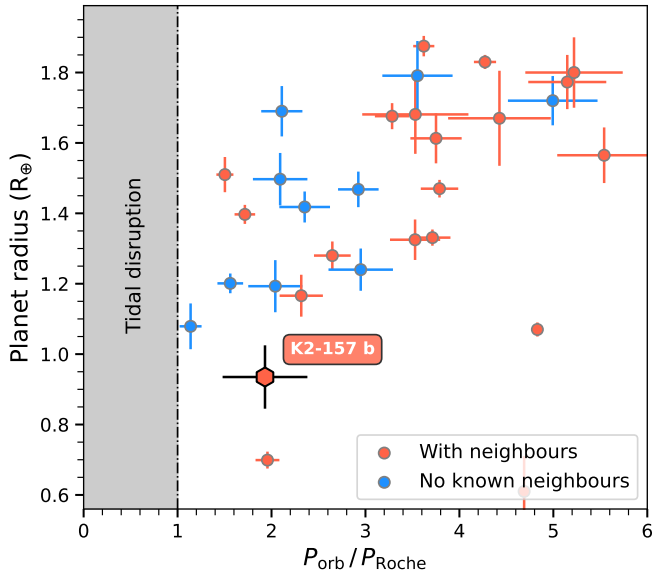


Fig. 11. Planet radius versus orbital period scaled to the Roche limit for USP rocky planets. The vertical line indicates the tidal disruption limit. Data: NASA Exoplanet Archive (24/03/2025).

target to search for signatures of orbital decay (see Fig. 11). Unfortunately, the long cadence of the K2 light curve combined with the low S/N of the individual transits and short time span of the observations prevent a meaningful search for orbital decay.

Going back to the period-radius parameter space, in Fig. 10 we colour the planets according to the stellar radii to illustrate an interesting trend that emerged over the last years: the shortest-period USP planets tend to orbit late-type stars (e.g. Ofir & Dreizler 2013; Rappaport et al. 2013; Smith et al. 2018; Barragán et al. 2018; Adams et al. 2021; Lam et al. 2021; Dai et al. 2024). Interestingly, K2-157, with a stellar radius of $R_\star$ = 0.860 ± 0.019 $R_\odot$, apparently contrasts with this trend. Other similar early-type stars hosting particularly close-in USP planets are K2-141 b (P_{orb} = 0.28 d, $R_\star$ = 0.68 $R_\odot$; Bonomo et al. 2023), TOI-2260 b (P_{orb} = 0.35 d, $R_\star$ = 0.94 $R_\odot$; Giacalone et al. 2022), and Kepler-78 b (P_{orb} = 0.36 d, $R_\star$ = 0.75 $R_\odot$; Bonomo et al. 2023). In the following, we study this trend and contextualise K2-157 b in this parameter space.

5.1.2. The semi-major axis dependency on spectral type

Adams et al. (2021) found that the semi-major axis of USP planets and the radius of their host stars are linearly correlated. We here aim to contextualize K2-157 b in the $a - R_\star$ space, revisit the correlation by considering the current planet sample, study whether it still holds when restricting to the small (R_p < 2 $R_\oplus$) USP planet population, try to quantify how much it is affected by observational bias, and discuss its possible origin.

We first used a Markov chain Monte Carlo (MCMC) ensemble sample (Goodman & Weare 2010) as implemented in `emcee`[24] (Foreman-Mackey et al. 2013) to sample the posterior probability density function of the coefficients A and B of a linear model, $y = Ax+B$[25]. For the complete USP sample, we obtain $A = 0.00918^{+0.00088}_{-0.00091}$ and $B = 0.00692^{+0.00068}_{-0.00064}$. For the small USP planet sample (R_p < 2 $R_\oplus$), we obtain $A = 0.00907^{+0.00098}_{-0.00102}$ and $B = 0.00682^{+0.00073}_{-0.00068}$. The inferred slopes are compatible and differ from zero at the 10.3σ and 9.1σ levels. Therefore, we conclude that the $a - R_\star$ correlation holds for small USP planets. In Fig. A.8, we show the $a - R_\star$ distribution of the two samples together with a set of posterior models. We also tested separately fitting the samples of USP planets with and without neighbours, and found no statistical differences.

We aim to examine whether the $a - R_\star$ correlation for small USP planets reflects a true feature of the exoplanet distribution, or if it could be driven by observational bias. Most USP planets have been detected through space-based photometers, so they are mostly affected by transit bias. Non-transiting configurations are a major bias of transit surveys, and it is particularly relevant for the USP population given their short orbital distances in comparison with the stellar radii. In Fig. 12 (left panel), we plot the $a - R_\star$ distribution of rocky USP planets together with different transit iso-probability lines. While there are several USP detections in the lower-left region of the diagram, where the transit probabilities range from ≃7% to ≃30%, there is a clear scarcity of USP planets in the lower-right region, where the probabilities range from ≃40% to ≃80%. We note that the transit S/N around larger hosts are lower. However, this can be arguably discarded as the cause of this lack of planets, given the large number of detections at larger orbital separations, which, in addition, statistically generate lower S/N signals given the lower number of detectable transit events. Therefore, we conclude that the lack of planets in the highlighted region of the left panel of Fig. 12, $a \lessapprox 0.0085$ au (1.8 $R_\odot$) and $R_\star \gtrapprox 0.5$ $R_\odot$, cannot be explained through observational bias, thus requiring a physical explanation. On the opposite side of the diagram (i.e. upper-left region), there is also a lack of planets. This region has a low transit probability when compared to the whole USP population (i.e. <10%), and more distant planets produce lower S/N transit signals, so we cannot directly assess whether this lack of planets reflects a true property of the exoplanet distribution. A more comprehensive study of planet occurrences would be necessary.

We studied whether tidal disruption could instead determine the closest orbits of USP planets across stellar types. The Roche limit scales linearly with the stellar radius, so it is reasonable to think that the closest USP planets orbit at larger orbital distances around earlier-type stars. We computed P_{Roche}[26] (Eq. (4)) for the known planet population to test whether the $a - R_\star$ trend holds after accounting for the minimum possible orbital distances in different stellar regimes. As we can see in Fig. 12 (right panel), the trend does not hold. There is not a lack of small P_{orb}/P_{Roche} ratios in early-type stars when compared to late-type stars, and instead we identify several ratios as short as $P_{orb}/P_{Roche} \sim 1.5-2$ distributed across a wide range of stellar radii, from ∼0.2 $R_\odot$ to ∼1 $R_\odot$. Hence, we interpret the $a - R_\star$ trend in the shortest orbits of rocky planets as a direct consequence of the dependency between the Roche limit and the stellar radius.

In all, the analyses presented above suggest that the distribution of the closest USP planets is not necessarily determined by the inner edges of the original proto-planetary discs, but simply by the present-day separation from the Roche limit, regardless of the spectral type. This aligns very well with the main formation theories of USP planets, which propose that their present-day orbits are primarily determined by their original migration triggered by interactions with outer companions and a subsequent orbital shrinkage that takes place before their final disruption.

[24] Available at https://github.com/dfm/emcee

[25] y corresponds to the semi-major axis and x to the stellar radius. A has units of $R_\odot^{-1}$ and B has units of au.

[26] We use P_{Roche} instead of a_{Roche} since it allows us to decrease the error budget by cancelling out the stellar mass and radius, but we note that exchanging these magnitudes has no effect in this analysis.

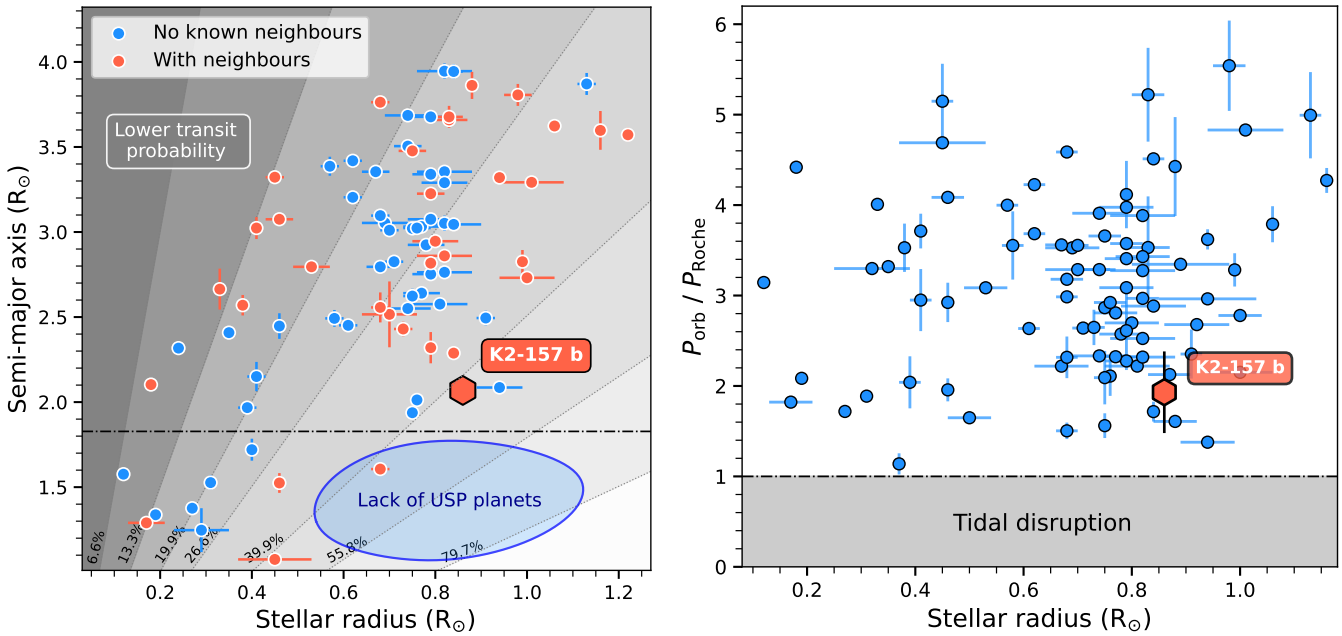


Fig. 12. Left: semi-major axis versus stellar radius of small USP planets ($R_p < 2$ R$_\oplus$), where we highlight a lack of planets that cannot be explained through observational bias, $a \lessapprox 0.0085$ au (1.8 R$_\odot$) and $R_\star \gtrapprox 0.5$ R$_\odot$. The dotted grey lines trace iso-probability transit regions. Right: orbital period scaled to the Roche limit for USP rocky planets versus the stellar radius of their host stars, where we can appreciate how the scaled orbital locations do not depend on the stellar spectral types. The horizontal line indicates the tidal disruption limit. Data: NASA Exoplanet Archive (24/03/2025).

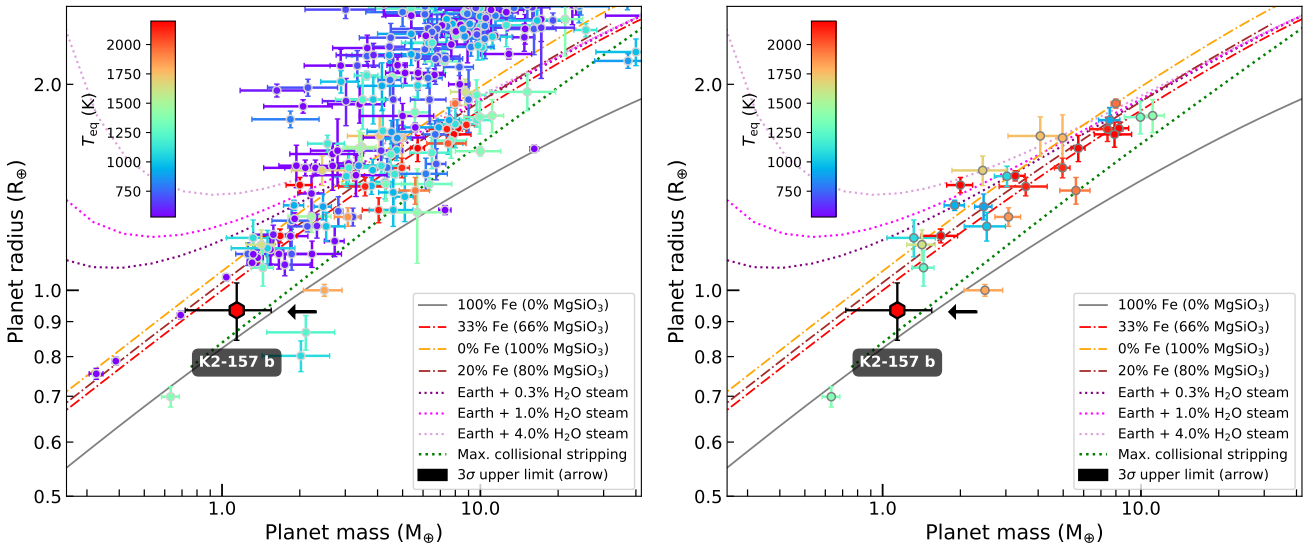


Fig. 13. Mass-radius diagram of all small planets (left) and USP planets (right) with masses and radii constrained to a precision better than 35 and 20%, respectively. The colour code represents the measured equilibrium temperatures. In both panels, we represent different composition curves for rocky planets derived in Marcus et al. (2010); Zeng et al. (2016, 2019); Turbet et al. (2020). The black arrow indicates the 3σ upper limit of K2-157 b's mass: 2.3 M$_\oplus$. Data: NASA Exoplanet Archive (24/03/2025). This plot was generated with `mr-plotter` (https://github.com/castro-gzlz/mr-plotter; Castro-González et al. 2023).

5.1.3. Mass-radius diagram

In Fig. 13, left panel, we contextualise K2-157 b (both the 1σ error bars and 3σ mass upper limit) in the mass-radius diagram of all small planets with masses and radii constrained to precisions better than 35% and 20%, respectively. In the right panel, we show the same diagram restricted to small USP planets. At a population level, we can see that planets with $R_p \lessapprox 1.8$ R$_\oplus$ are consistent with an Earth-like bulk composition (i.e. an iron-rich core making up ≃33% of the planetary mass and a silicate-dominated mantle composing the remaining ≃66%; Zeng et al. 2019). However, the wealth of precise mass measurements over the last years has revealed a non-negligible fraction of rocky planets with higher densities (e.g. Lam et al. 2021; Santerne et al. 2018; Azevedo Silva et al. 2022). These planets are thought to have a larger iron-to-silicate mass fraction

(i.e. larger cores or smaller mantles) than Earth, which could be due to a high metal content in the original proto-planetary disc (e.g. Grasset et al. 2009) or to catastrophic giant impacts (e.g. Chambers 2004) that strip away a significant fraction of the mantle (e.g. Marcus et al. 2010).

K2-157 b lies between the Earth-like and pure iron composition curves (Zeng et al. 2019), with 1σ uncertainties compatible with both models. Therefore, our mass and radius measurements indicate that K2-157 b may have a larger iron-to-silicate mass fraction than Earth. Adibekyan et al. (2021) found that stellar abundances and planet densities of highly irradiated rocky planets are correlated, suggesting a star-planet connection that may reflect the composition of the original proto-planetary discs. We used the [Fe/H], [Mg/H], and [Si/H] stellar abundances (Sect. 3, Table 3) and followed the stoichiometric model from Santos et al. (2015, 2017) to predict the iron-to-silicate mass fraction present in the original proto-planetary disc. We find a value compatible with that of the proto-solar disc (i.e. $f_{\rm iron}^{\rm star} = 30.5 \pm 2.8\%$). Therefore, in case K2-157 b has a considerably higher density than the expected for an Earth-like composition, it will not be easily explained through a primordial iron enhancement, and would thus possibly require the existence of a large-scale mantle-stripping impact (e.g. Bonomo et al. 2019).

Additional high-precision RV and photometric data are necessary to determine whether K2-157 b is denser than Earth, and to precisely estimate its iron-to-silicate mass fraction. In particular, our stellar characterization imposes a radius and mass uncertainty floor of 0.021 $R_\oplus$ and 0.024 $M_\oplus$, respectively, in contrast to our derived uncertainties of 0.090 $R_\oplus$ and 0.42 $M_\oplus$, so the mass of K2-157 b still has a large room for improvement. We note, however, that while imprecise in relative terms, the mass measurement presented here still has a considerable statistical value. As we can see in Fig. 13, the current mass-radius diagram is practically devoid of planets at $R_{\rm p} \lessapprox 1$ $R_\oplus$, even when considering a relaxed mass precision threshold (i.e. $\delta M_{\rm p}/M_{\rm p} < 35\%$). It is widely assumed that Earth and sub-Earth-sized planets broadly follow the Earth-like composition model, similarly to larger planets, and in consequence typically have rocky compositions. However, this inference is still based on a very limited observational evidence (i.e. the Earth, Venus, Mars, and the TRAPPIST-1 system; Gillon et al. 2017, 2016; Agol et al. 2021). Hence, the mass constraint on K2-157 b, although not very precise, still brings further evidence on the likely rocky nature of the smallest planets in our Galaxy. Interestingly, the rocky surfaces of small planets with equilibrium temperatures ($T_{\rm eq}$) above ≃1800 K are expected to be completely melted, forming a 'magma ocean' (irrespective of whether they host an atmosphere or not; Lichtenberg & Miguel 2025). K2-157 b, with a $T_{\rm eq}$ of 2432 ± 42 K, is expected to have one of the hottest dayside temperatures of the current sample of USP with constrained masses, thus being an excellent candidate to be a true 'lava world'. Future characterization of K2-157 b may thus be able to probe planetary thermodynamic regimes that are inaccessible in the present-day Solar System, providing a fantastic test bed for the transition from primary to secondary atmospheres presumably happening in young rocky planets cooling down from primordial heating (e.g. Kite & Barnett 2020; Tian & Heng 2024).

5.2. K2-157 c and K2-157 d in context: Period-mass diagram of neighbours of USP planets

In Fig. 14, we contextualise K2-157 c and d in the period-mass diagram of known planets, where we highlight the current sample of neighbours of USP planets[27]. These 78 planets occupy a wide region of the parameter space, showing masses from sub-Earths to super-Jovians and orbital periods from a few days to thousands of days. However, the vast majority of these planets (i.e. 83% of the current sample) lie within the sub-Neptune regime, showing a distribution in qualitative agreement with the overall planet distribution (e.g. Mayor et al. 2011; Howard et al. 2012; Hsu et al. 2019; Dattilo & Batalha 2024). The well-known planet occurrence drop occurring roughly at Neptune's mass (i.e. $M_{\rm p} \simeq 17$ $M_\oplus$) is thus seemingly preserved within the observed distribution of companions to USP planets. In this context, K2-157 c and K2-157 d are both located in the poorly populated upper part of the period-mass space, in a warm region identified as the Neptunian savanna[28] (Bourrier et al. 2023), which, as we can see in Fig. 14, is practically devoid of neighbours of USP planets. Interestingly, the only two known neighbours of USP planets in the warm savanna (i.e. 55 Cnc c and 55 Cnc f; McArthur et al. 2004; Fischer et al. 2008; Bourrier et al. 2018a) also belong to the same planetary system, 55 Cnc, which we highlight in Fig. 14 together with K2-157 c and K2-157 d. Therefore, the system K2-157, having a USP planet accompanied by two neighbours in the warm savanna, of which the closer-in has a slightly higher minimum mass than the most distant one, and being possibly accompanied by an additional long-period giant planet (see Sect. 4.2), becomes the most similar system to the iconic 55 Cnc system. We note, however, that 55 Cnc has an additional non-transiting Jupiter-mass planet between the USP planet and the two savanna neighbours (i.e. 55 Cnc b, see Fig. 14), whose presence in the K2-157 system can be safely discarded based on our derived RV sensitivity limits (Sect. 4.6 and Fig. 9).

The unusual locations of K2-157 c and d in the period-mass parameter space can provide relevant clues on their evolution. Gas-rich and/or ice-rich giant planets such as K2-157 c and K2-157 d are widely thought to form at large orbital distances, beyond the ice line, and subsequently migrate inwards. Interestingly, the mere co-existence of two giant planets in relatively close-in orbits (i.e. within the ice line) favours the so-called disc-driven migration hypothesis[29] in contrast to the alternative HEM theory[30] to explain the origins of these planets. Disc-driven migration can deliver giant planets with companions[31] (e.g. Malhotra 1993; Lee & Peale 2002; Raymond et al. 2006), while HEM is expected to remove any planet situated within the orbit of the migrating giant (e.g. Mustill et al. 2015), which would make it difficult to generate the observed configuration in K2-157. There are also increasing observational constraints

[27] Most neighbours of USP planets do not have mass measurements. For planets with only radius measurements, we estimated their masses through the relations from Chen & Kipping (2017). The massive and/or wide-orbit planets K2-187 e (Mayo et al. 2018) and WASP-47 b, c, and d (Hellier et al. 2012) fall outside the limits of the plot.

[28] The term 'savanna' refers to the milder deficit of planets in this region compared to that in the Neptunian desert (Benítez-Llambay et al. 2011; Szabó & Kiss 2011; Youdin 2011).

[29] An early migration through the proto-planetary disc before the gas dissipates (e.g. Goldreich & Tremaine 1979; Lin et al. 1996).

[30] An inward migration caused by a massive stellar or planetary companion that highly excites the planet eccentricity −making it lose orbital momentum− and whose orbit is subsequently shrunken and circularized due to stellar tides −making it lose energy (e.g. Wu & Murray 2003; Chatterjee et al. 2008; Correia et al. 2011).

[31] These planets are expected to originally make up resonant configurations, but they also have the potential to evolve and escape the resonance (Goldreich & Schlichting 2014), which could have been the case for K2-157 c and K2-157 d.

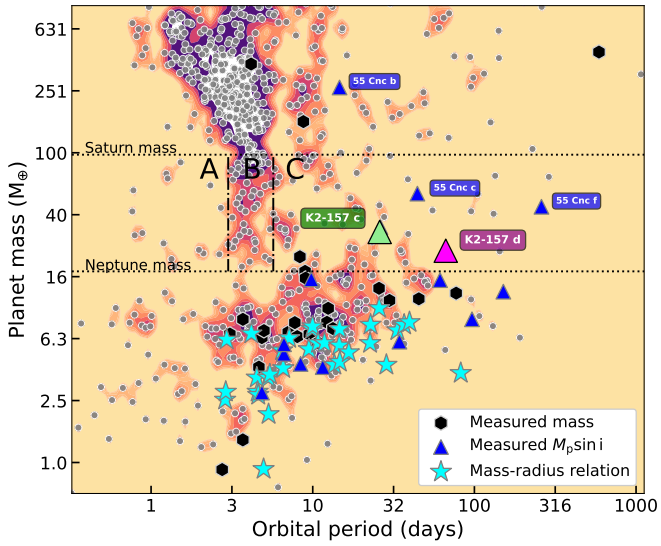


Fig. 14. Contextualization of K2-157 c and K2-157 d in the period-mass diagram of known exoplanets with masses constrained to a precision better than 30%. Black hexagons, blue triangles, and light-blue stars represent the current sample of known neighbours of USP planets. The delimited regions A, B, and C, represent the boundaries of the Neptunian desert, ridge, and savanna in the super-Neptune and sub-Jovian domains (Castro-González et al. 2024a). Data: NASA Exoplanet Archive (24/03/2025). This plot was generated with `nep-des` (`https://github.com/castro-gzlz/nep-des`).

that suggest that intermediate planets in the warm savanna were preferentially brought inwards through disc-driven migration, in contrast to closer-in hot Neptunes, which might have been primarily brought through HEM towards the Neptunian ridge (see Correia et al. 2020; Bourrier et al. 2023; Castro-González et al. 2024a,b; Vissapragada & Behmard 2025).

5.3. Orbital stability and constraints

The K2-157 system is composed of an Earth-mass planet ($M_{p,b} \approx 1.14$ M$_\oplus$) with a USP orbit ($P_{orb,b} \approx 8.8$ h), and two super-Neptune-mass planets ($M_{p,c} \approx 30.8$ M$_\oplus$, $M_{p,d} \approx 23.3$ M$_\oplus$) further away, in the vicinity of a 5:2 mean motion resonance ($P_{orb,d}/P_{orb,c} \approx 2.563$). While the mass of the innermost planet is relatively well estimated from RV measurements, the masses of the other two planets correspond to minimal estimations, since the inclinations of their orbits are unknown. The eccentricities are also loosely constrained from RV measurements.

To inspect the stability of the system and derive constraints for the unknown orbital parameters, we performed a dynamical analysis as in previous works (e.g. Correia et al. 2005, 2010). The full system was integrated around the best fit (Table B.5), varying two orbital parameters on a uniform grid of initial conditions. Each initial condition was integrated for 10 000 yr, using the symplectic integrator SABAC4 (Laskar & Robutel 2001), with a step size of 2.5×10^{-5} yr and general relativity corrections. We then performed a frequency analysis (Laskar 1990, 1993) of the mean longitude of K2-157 d over two consecutive time intervals of 5 000 yr, and determined the main frequency, n and n', respectively. The stability was measured with $\Delta = |1 - n'/n|$, which estimates the chaotic diffusion of the orbits.

We first explored the stability of the system by varying the orbital period and the eccentricity of K2-157 d (Fig. 15). The results are reported in colour: white and yellow correspond to strongly chaotic unstable trajectories, while red and black give extremely stable quasi-periodic orbits on Gyr timescales. We observe that the best fit solution from Table B.5 (marked with a blue dot) is completely stable, even for eccentricities up to 0.3. We can also clearly identify a V-shape structure on the left-hand side of Fig. 15 corresponding to the 5:2 mean motion resonance with K2-157 c. Since the current best fit is completely outside this region, we conclude that the two planets are not in resonance, even for higher eccentricity values. We additionally note that the system is on the correct side of the resonance predicted by planetary migration models (e.g. Lissauer et al. 2011). This feature strengthens the hypothesis that the USP planet K2-157 b also formed further away and then migrated inwards.

In a second experiment, we varied the eccentricities of the two super-Neptune-mass planets (Fig. 16). These two eccentricities were not constrained by the best fit solution (Table B.5), but can play an important role in the stability of the system. Indeed, we observe that high eccentricity values of both planets can lead to unstable orbits, although the system remains stable as long as $e_c \lesssim 0.35$ and $e_d \lesssim 0.3$. We then conclude that the K2-157 planetary system is very resilient to the uncertainties in the determination of the eccentricities.

The RV technique alone is unable to constrain the inclination, i, and the longitude of the node, Ω, of the planets. Therefore, in a final experiment, we vary these two parameters for the outermost planet K2-157 d (Fig. 17). We observe that the system is stable within a circle centred at the coplanar solution, which corresponds to mutual inclinations smaller than 60° between the orbit of K2-157 d and the orbits of the remaining two planets in the system[32]. As we change the inclination, the mass of the outer planet increases. At the boundary of stability circle, $i_d = 90° \pm 60°$, we get a maximum mass for K2-157 d of about twice its minimum value (i.e. $M_{d,max} \approx 47$ M$_\oplus$). A similar constraint could be derived for the maximal mass of K2-157 c (i.e. $M_{c,max} \approx 62$ M$_\oplus$). Indeed, we can also get a maximal mutual inclination of 60° with $\Omega_d = \pm 60°$ and $i_d = 90°$ (Fig. 17), for which the mass of K2-157 d is minimal ($M_d = 23.3$ M$_\oplus$). That is, the main source of instability results from mutual inclinations above the 60° threshold and not from the increase in the masses.

5.4. Comparison to formation mechanisms of USP planets

Formation theories of USP planets typically require the existence of outer planetary companions that brought them towards their present-day orbits. However, there is no consensus on the predominant mechanism triggering this likely migration. In this section, we briefly introduce three promising theories and compare their predictions to the properties of K2-157.

5.4.1. High-eccentricity migration

Petrovich et al. (2019) propose that USP planets were originally formed at orbital periods of ~5–10 d (~0.05–0.1 au) and reached their current orbits through HEM. Chaotic interactions with outer planetary companions would significantly increase the eccentricities of these planets (e.g. $1-e \ll 1$). Subsequently, energy dissipation from tides raised by the star on the planets would shrink and circularise their orbits. This theory is closely related to the secular chaos theory proposed to explain the short orbits of hot Jupiters (e.g. Wu & Lithwick 2011). The initial conditions required to form USP planets through this channel are

[32] Additional stability regions also exists around ($\Omega_d = 180°$, $i_d = 90°$), but they are not shown in Fig. 17 because they correspond to retrograde orbits, which are more unlikely from a formation point-of-view.

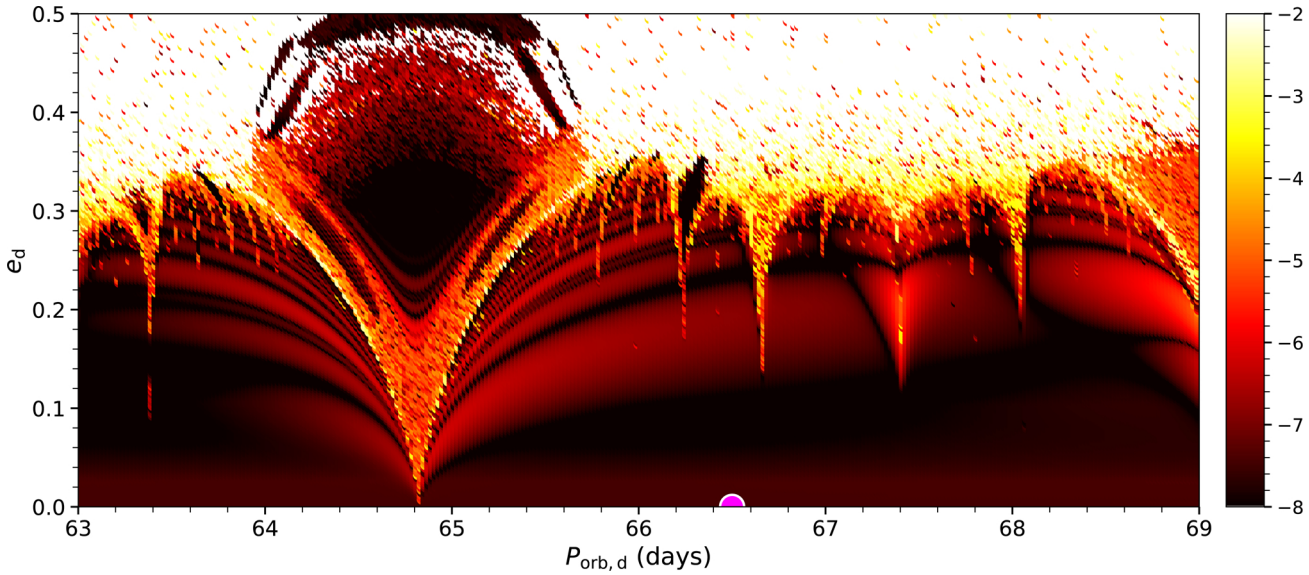


Fig. 15. Stability analysis of the K2-157 planetary system. For fixed initial conditions (Table B.5), the parameter space of the system is explored by varying the orbital period and eccentricity of K2-157 d. The step size is 0.02 d in orbital period and 0.0025 in eccentricity. For each initial condition, the system was integrated over 10^4 yr and a stability indicator was calculated, which involved a frequency analysis of the mean longitude of the inner planet. The chaotic diffusion is measured by the variation in the frequency. White-yellow points correspond to highly unstable orbits, while red points correspond to stable orbits on Gyr timescales. The magenta dot corresponds to the best-fit solution ($P_{orb,d}$ = 66.50 d, e_d = 0).

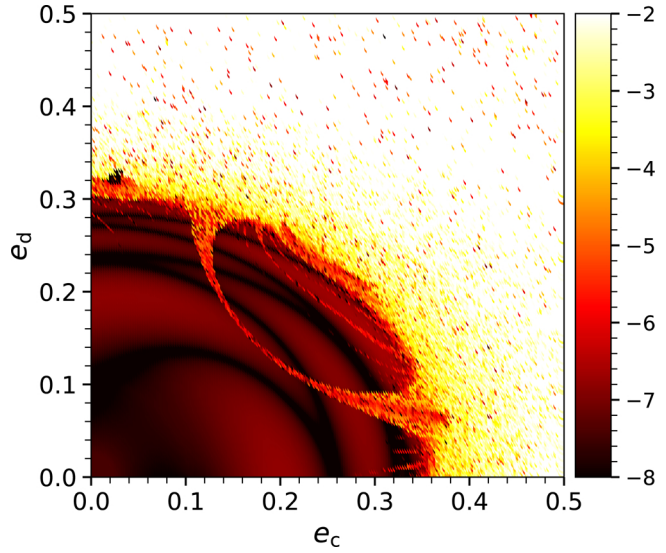


Fig. 16. Stability analysis of the K2-157 system in the plane (e_c, e_d), assuming coplanar orbits. For fixed initial conditions (Table B.5), the parameter space is explored by varying the eccentricities of K2-157 c and K2-157 d with a step size of 0.0025. The stability index and colour codes are obtained as for Fig. 15.

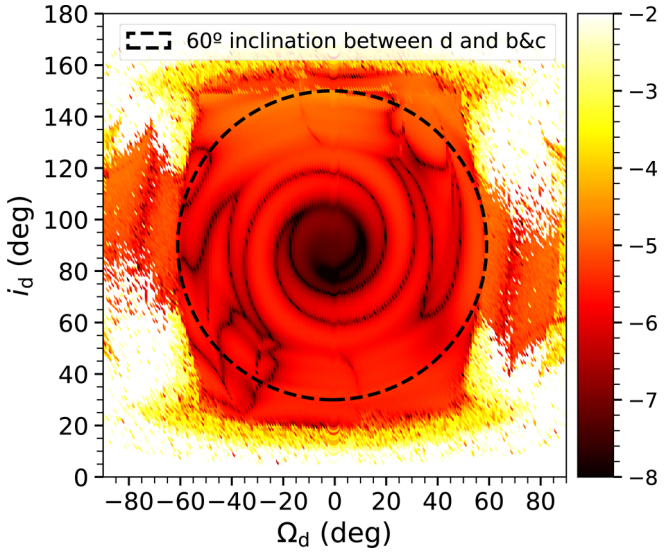


Fig. 17. Stability analysis of the K2-157 system in the plane (Ω_d, i_d). For fixed initial conditions (Table B.5), the parameter space is explored by varying the longitude of the node Ω_d and the inclination i_d of the outer planet, with a step size of 1°. The stability index and colour codes are obtained as for Fig. 15.

the existence of several neighbours (typically ≥3) and moderate eccentricities and/or inclinations (e_{rms}, i_{rms} ∼ 0.1) able to drive chaotic diffusion.

This mechanism predicts that neighbours of USP planets should have extended orbits, from tens of days (i.e P_{orb} > 10 d) up to beyond ∼au distances, as well as relatively large period ratios between adjacent planets (typically P_i / P_{i+1} ≳ 3). In addition, the outer neighbours need to be considerably more massive than the USP planets (typically ≳10 $M_\oplus$). This mechanism also predicts mutual spin-orbit angles and inclinations between the USP and the outer planets in the range of ∼10–50°. When compared to K2-157, the relatively large orbits and masses of the neighbours K2-157 c and K2-157 d agree with the predictions of this mechanism. In addition, the measured ratio $P_c/P_d \simeq 2.6$ is near the typical value, and the subsequent ratio would be considerably larger in case the quadratic trend in the RVs corresponds to an outer massive companion. Regarding the mutual inclinations, our orbital stability analysis indicates that inclinations below ∼60° in K2-157 result in a dynamically stable system, regardless of the true masses of K2-157 c and K2-157 d (Sect. 5.3), which is compatible with the predicted range of inclinations from this mechanism.

5.4.2. Low-eccentricity migration

Pu & Lai (2019) propose that USP planets originally formed in closer-in orbits, at orbital periods of ∼1–3 d (∼0.02 and 0.04 au), and were then brought inwards through a low-eccentricity migration mechanism (LEM). This mechanism relies upon the combination of secular interactions and tidal dissipation (e.g. Wu & Goldreich 2002; Mardling 2007, 2010). Contrary to the HEM mechanism, LEM requires the existence of a multi-planet system with typically ≥2 neighbours, and requires the inner planet to achieve mild eccentricities ($e \sim 0.05$–0.2) before entering the tidal decay process. Therefore, regarding the initial conditions, LEM requires more constrained proto-USP periods, but requires fewer neighbours to trigger their migration.

The LEM mechanism allows for more relaxed properties of USP-hosting systems than the HEM mechanism. Exterior neighbours can be less massive (i.e. $\gtrsim$3 $M_\oplus$) and there is no need for large values of P_i / P_{i+1}. As was discussed before, the mass condition is well met in the K2-157 system. In addition, LEM predicts milder mutual inclinations than HEM, of about 20°, which is compatible with our dynamical stability analysis.

From the comparisons discussed above, we conclude that K2-157 is perfectly compatible with the relaxed constraints of the LEM mechanism, but so it is with the more restrictive predictions of the HEM mechanism, thus converting these two theories into promising contenders to explain its origin. We also note that these two eccentricity-based mechanisms may expect some degree of eccentricity enhancements for the companion planets in USP systems, which is allowed by the RVs ($e_c < 0.2$ and $e_d < 0.5$ at 3σ) and stability analysis (e_c, $e_d \lesssim 0.3$) of this system.

5.4.3. Obliquity-driven migration

Millholland & Spalding (2020) propose that USP initially come from orbits $\lesssim$0.04–0.05 au and arrive into their present-day locations through obliquity-driven tidal migration. This mechanism states that the spin of proto-USP planets first locks on an equilibrium configuration, called Cassini state 2, due to tidal dissipation. Then, the planetary obliquity is significantly enhanced and the planet starts migrating inwards, which would generate an even larger obliquity, entering a process of runaway orbital decay that stops when the Cassini state 2 is destabilised.

Contrary to the HEM and LEM eccentricity-based mechanisms, the obliquity-driven tidal migration is most efficient when the planetary neighbours have close-in orbits, typically with periods $P_{orb} < 10$ d. This observational prediction contrasts with the substantially larger periods of planets K2-157 c and K2-157 d. We note, however, that for $P_{orb} \lesssim 10$ d, our RV sensitivity analysis only discards the existence of additional planets with $M_p \gtrsim$ 4–5 $M_\oplus$ (Sect. 4.6), so there is still room for the existence of non-transiting smaller planets in this close-in orbital region which could have been responsible for the obliquity-driven migration of K2-157 b.

6. Summary and conclusions

We acquired 49 ESPRESSO spectra to confirm and characterize the USP ($P_{orb} = 8.8$ h) Earth-sized ($R_p = 0.935 \pm 0.090$ $R_\oplus$) planet K2-157 b, as well as to constrain the presence of additional companions in the system. We first derived the stellar parameters of K2-157 through a high-resolution, high-S/N spectrum obtained from the co-adding of the individual ESPRESSO spectra. We find that K2-157 is a G9 V star with $T_{eff} = 5334 \pm 64$ K, $R_\star = 0.860 \pm 0.019$ $R_\odot$, and $M_\star = 0.890 \pm 0.029$ $M_\odot$, in agreement with previous estimations. A blind-search analysis of the ESPRESSO RVs revealed the existence of two additional Keplerian signals in the system, which, after discarding stellar activity as their possible origin, we confirm as planets: K2-157 c ($P_{orb,c} = 25.942^{+0.045}_{-0.044}$ d, $M_{p,c} \sin i = 30.8 \pm 1.9$ $M_\oplus$), and K2-157 d ($P_{orb,d} = 66.50^{+0.71}_{-0.59}$ d, $M_{p,d} \sin i = 23.3 \pm 2.5$ $M_\oplus$). This analysis also revealed the existence of a long-term quadratic trend that could be due to an additional long-period massive companion or, alternatively, reflect the magnetic cycle of the star.

A joint analysis of the K2 and ESPRESSO data allowed us to infer the properties of the system. This analysis constrained the mass of K2-157 b at the 2.7σ level, $M_{p,b} = 1.14^{+0.41}_{-0.42}$ $M_\oplus$ (<2.4 $M_\oplus$ at 3σ), which makes the planet compatible with a rocky composition with a likely (68% confidence) higher iron-to-silicate mass fraction than Earth. K2 and TESS photometry did not allow us to determine whether K2-157 d transits its star, but K2 data allowed us to discard non-grazing transit configurations for K2-157 c ($i_c < 88.4°$ at 3σ). ESPRESSO data also allowed us to constrain the eccentricities of K2-157 c and d: $e_c < 0.2$ and $e_d < 0.5$ at 3σ. In this regard, we performed a dynamical analysis that showed that the system is stable for eccentricities up to e_c, $e_d \sim 0.3$ and mutual inclinations up to ∼60°. Therefore, both the observations and stability analysis discard highly eccentric orbits for the outer planetary companions but are still compatible with moderate eccentricities up to ∼0.2−0.3.

The orbital architecture of K2-157 (a USP planet accompanied by massive neighbours in the warm Neptunian savanna) is infrequent, with only one other similar case reported to date: the iconic 55 Cnc system. Whether these systems are intrinsically unusual or the low observed occurrence is dominated by observational bias needs to be studied. Interestingly, the USP planets of these systems, which have massive ($M_p > 10$ $M_\oplus$), long-period ($P_{orb} > 10$ d), relatively spaced (P_i / $P_{i+1} \gtrsim 3$), and possibly misaligned planetary neighbours, could have migrated inwards through a HEM process triggered by chaotic secular interactions. A LEM process could have also played a role.

K2-157 b has one of the shortest orbits known to date. This characteristic makes the K2-157 system particularly interesting when considering the early G9 V spectral type of the host star, given that the rocky planets with the shortest orbits are preferentially found around late-type stars. We further studied this trend and found that it cannot be explained through observational bias, thus requiring a physical explanation. We also found that this trend does not hold when scaling the orbital separation to the Roche limit. Instead, we identify a featureless distribution across a wide range of spectral types, which leads us to interpret the trend as a direct consequence of the dependency between the Roche limit and the stellar radius. We thus conclude that the distribution of the closest USP planets is not necessarily determined by the inner edges of the original proto-planetary discs, as was previously suggested, but simply by the present-day separation from the Roche limit, regardless of the spectral type of the host star. This explanation aligns very well with the main formation theories of USP planets, according to which their present-day orbits are primarily determined by the original interactions with outer companions and subsequent tidal decay, with no preservation of signatures of their primordial distribution across the proto-planetary discs.

Data availability

Full Tables B.1–B.3 are available at the CDS via anonymous ftp to cdsarc.cds.unistra.fr (130.79.128.5)

or via https://cdsarc.cds.unistra.fr/viz-bin/cat/J/A+A/699/A344

Acknowledgements. We are very grateful to the reviewer, who provided insightful suggestions that improved the quality of this work. A.C.-G. is funded by the Spanish Ministry of Science through MCIN/AEI/10.13039/501100011033 grant PID2019-107061GB-C61. A.C.M.C. acknowledges support from the FCT, Portugal, through the CFisUC projects UIDB/04564/2020 and UIDP/04564/2020, with DOI identifiers 10.54499/UIDB/04564/2020 and 10.54499/UIDP/04564/2020, respectively. This research is co-funded by the European Union (ERC, FIERCE, 101052347). Views and opinions expressed are however those of the author(s) only and do not necessarily reflect those of the European Union or the European Research Council. Neither the European Union nor the granting authority can be held responsible for them. This work was supported by FCT - Fundação para a Ciência e a Tecnologia through national funds by these grants: UIDB/04434/2020 DOI: 10.54499/UIDB/04434/2020, UIDP/04434/2020 DOI: 10.54499/UIDP/04434/2020. J.I.G.H. and A.S.M. acknowledge financial support from the Spanish Ministry of Science, Innovation and Universities (MICIU) projects PID2020-117493GB-I00 and PID2023-149982NB-I00. The INAF authors acknowledge financial support of the Italian Ministry of Education, University, and Research with PRIN 201278X4FL and the "Progetti Premiali" funding scheme. This work was financed by Portuguese funds through FCT (Fundação para a Ciência e a Tecnologia) in the framework of the project 2022.04048.PTDC (Phi in the Sky, DOI 10.54499/2022.04048.PTDC). C.J.M. also acknowledges FCT and POCH/FSE (EC) support through Investigador FCT Contract 2021.01214.CEECIND/CP1658/CT0001 (DOI 10.54499/2021.01214.CEECIND/CP1658/CT0001). We acknowledge financial support from the Agencia Estatal de Investigación of the Ministerio de Ciencia e Innovación MCIN/AEI/10.13039/501100011033 and the ERDF "A way of making Europe" through project PID2021-125627OB-C32, and from the Centre of Excellence "Severo Ochoa" award to the Instituto de Astrofisica de Canarias. F.P.E. would like to acknowledge the Swiss National Science Foundation (SNSF) for supporting research with ESPRESSO through the SNSF grants nr. 140649, 152721, 166227, 184618 and 215190. The ESPRESSO Instrument Project was partially funded through SNSF's FLARE Programme for large infrastructures. This publication made use of `TESS-cont` (https://github.com/castro-gzlz/TESS-cont), which also made use of `tpfplotter` (Aller et al. 2020) and `TESS_PRF` (Bell & Higgins 2022). This work made use of `mr-plotter` (available in https://github.com/castro-gzlz/mr-plotter).

References

Adams, E. R., Jackson, B., Johnson, S., et al. 2021, PSJ, 2, 152
Adibekyan, V. Z., Sousa, S. G., Santos, N. C., et al. 2012, A&A, 545, A32
Adibekyan, V., Figueira, P., Santos, N. C., et al. 2015, A&A, 583, A94
Adibekyan, V., Dorn, C., Sousa, S. G., et al. 2021, Science, 374, 330
Agol, E., Dorn, C., Grimm, S. L., et al. 2021, PSJ, 2, 1
Akeson, R. L., Chen, X., Ciardi, D., et al. 2013, PASP, 125, 989
Aller, A., Lillo-Box, J., Jones, D., Miranda, L. F., & Barceló Forteza, S. 2020, A&A, 635, A128
Ambikasaran, S., Foreman-Mackey, D., Greengard, L., Hogg, D. W., & O'Neil, M. 2015, IEEE Trans. Pattern Anal. Mach. Intell., 38, 252
Angus, R., Morton, T., Aigrain, S., Foreman-Mackey, D., & Rajpaul, V. 2018, MNRAS, 474, 2094
Azevedo Silva, T., Demangeon, O. D. S., Barros, S. C. C., et al. 2022, A&A, 657, A68
Balsalobre-Ruza, O., Lillo-Box, J., Silva, A. M., et al. 2025, A&A, 694, A15
Baranne, A., Queloz, D., Mayor, M., et al. 1996, A&AS, 119, 373
Barragán, O., Gandolfi, D., Dai, F., et al. 2018, A&A, 612, A95
Barros, S. C. C., Demangeon, O. D. S., Alibert, Y., et al. 2022, A&A, 665, A154
Baycroft, T. A., Triaud, A. H. M. J., Faria, J., Correia, A. C. M., & Standing, M. R. 2023, MNRAS, 521, 1871
Bayes, M., & Price, M. 1763, Phil. Trans. R. Soc. London Ser. I, 53, 370
Behmard, A., Dai, F., Brewer, J. M., Berger, T. A., & Howard, A. W. 2023, MNRAS, 521, 2969
Bell, K. J., & Higgins, M. E. 2022, Astrophysics Source Code Library [record ascl:2207.008]
Benítez-Llambay, P., Masset, F., & Beaugé, C. 2011, A&A, 528, A2
Bensby, T., Feltzing, S., & Oey, M. S. 2014, A&A, 562, A71
Boley, K. M., Panero, W. R., Unterborn, C. T., et al. 2023, ApJ, 954, 202
Bonomo, A. S., Zeng, L., Damasso, M., et al. 2019, Nat. Astron., 3, 416
Bonomo, A. S., Dumusque, X., Massa, A., et al. 2023, A&A, 677, A33
Borucki, W. J., Koch, D., Basri, G., et al. 2010, Science, 327, 977
Boss, A. P. 1998, Ann. Rev. Earth Planet. Sci., 26, 53
Bouchy, F., Pepe, F., & Queloz, D. 2001, A&A, 374, 733
Bourrier, V., Dumusque, X., Dorn, C., et al. 2018a, A&A, 619, A1
Bourrier, V., Ehrenreich, D., Lecavelier des Etangs, A., et al. 2018b, A&A, 615, A117
Bourrier, V., Attia, M., Mallonn, M., et al. 2023, A&A, 669, A63
Brewer, B. J., Pártay, L. B., & Csányi, G. 2011, Stat. Comput., 21, 649
Buchhave, L. A., Latham, D. W., Johansen, A., et al. 2012, Nature, 486, 375
Buchner, J., Georgakakis, A., Nandra, K., et al. 2014, A&A, 564, A125
Castro-González, A., Demangeon, O. D. S., Lillo-Box, J., et al. 2023, A&A, 675, A52
Castro-González, A., Bourrier, V., Lillo-Box, J., et al. 2024a, A&A, 689, A250
Castro-González, A., Lillo-Box, J., Armstrong, D. J., et al. 2024b, A&A, 691, A233
Castro-González, A., Lillo-Box, J., Correia, A. C. M., et al. 2024c, A&A, 684, A160
Cauley, P. W., Shkolnik, E. L., Llama, J., & Lanza, A. F. 2019, Nat. Astron., 3, 1128
Chambers, J. E. 2004, Earth Planet. Sci. Lett., 223, 241
Chatterjee, S., Ford, E. B., Matsumura, S., & Rasio, F. A. 2008, ApJ, 686, 580
Chen, J., & Kipping, D. 2017, ApJ, 834, 17
Chen, S. S., Donoho, D. L., & Saunders, M. A. 1998, SIAM J. Sci Comp., 20, 33
Christiansen, J. L. 2022, Nat. Astron., 6, 516
Cointepas, M., Bouchy, F., Almenara, J. M., et al. 2024, A&A, 685, A19
Correia, A. C. M. 2014, A&A, 570, L5
Correia, A. C. M., Udry, S., Mayor, M., et al. 2005, A&A, 440, 751
Correia, A. C. M., Couetdic, J., Laskar, J., et al. 2010, A&A, 511, A21
Correia, A. C. M., Laskar, J., Farago, F., & Boué, G. 2011, Celest. Mech. Dyn. Astron., 111, 105
Correia, A. C. M., Bourrier, V., & Delisle, J. B. 2020, A&A, 635, A37
Czesla, S., Schröter, S., Schneider, C. P., et al. 2019, PyA: Python astronomy-related packages [record ascl:1906.010]
da Silva, L., Girardi, L., Pasquini, L., et al. 2006, A&A, 458, 609
Dai, F., Masuda, K., & Winn, J. N. 2018, ApJ, 864, L38
Dai, F., Masuda, K., Winn, J. N., & Zeng, L. 2019, ApJ, 883, 79
Dai, F., Howard, A. W., Batalha, N. M., et al. 2021, AJ, 162, 62
Dai, F., Howard, A. W., Halverson, S., et al. 2024, AJ, 168, 101
Damasso, M., Sozzetti, A., Lovis, C., et al. 2020, A&A, 642, A31
Damasso, M., Rodrigues, J., Castro-González, A., et al. 2023, A&A, 679, A33
Dattilo, A., & Batalha, N. M. 2024, AJ, 167, 288
Delisle, J. B., Hara, N., & Ségransan, D. 2020, A&A, 635, A83
Demangeon, O. D. S., Zapatero Osorio, M. R., Alibert, Y., et al. 2021, A&A, 653, A41
Deming, D., Knutson, H., Kammer, J., et al. 2015, ApJ, 805, 132
Demory, B.-O., Gillon, M., de Wit, J., et al. 2016, Nature, 532, 207
Dorn, C., & Lichtenberg, T. 2021, ApJ, 922, L4
Dransfield, G., Triaud, A. H. M. J., Guillot, T., et al. 2022, MNRAS, 515, 1328
Dressing, C. D., & Charbonneau, D. 2015, ApJ, 807, 45
Dumusque, X., Boisse, I., & Santos, N. C. 2014, ApJ, 796, 132
Fabrycky, D. C., Lissauer, J. J., Ragozzine, D., et al. 2014, ApJ, 790, 146
Fang, J., & Margot, J.-L. 2012, ApJ, 761, 92
Faria, J. P., Haywood, R. D., Brewer, B. J., et al. 2016, A&A, 588, A31
Faria, J. P., Santos, N. C., Figueira, P., & Brewer, B. J. 2018, J. Open Source Softw., 3, 487
Faria, J. P., Suárez Mascareño, A., Figueira, P., et al. 2022, A&A, 658, A115
Figueira, P., Marmier, M., Boué, G., et al. 2012, A&A, 541, A139
Figueira, P., Faria, J. P., Silva, A. M., et al. 2025, A&A, submitted
Fischer, D. A., Marcy, G. W., Butler, R. P., et al. 2008, ApJ, 675, 790
Foreman-Mackey, D., Hogg, D. W., Lang, D., & Goodman, J. 2013, PASP, 125, 306
Foreman-Mackey, D., Agol, E., Ambikasaran, S., & Angus, R. 2017, AJ, 154, 220
Fulton, B. J., Petigura, E. A., Blunt, S., & Sinukoff, E. 2018, PASP, 130, 044504
Gaia Collaboration (Vallenari, A., Brown, et al.) 2023, A&A, 674, A1
Gardner, J. P., Mather, J. C., Clampin, M., et al. 2006, Space Sci. Rev., 123, 485
Giacalone, S., Dressing, C. D., Hedges, C., et al. 2022, AJ, 163, 99
Gillon, M., Jehin, E., Lederer, S. M., et al. 2016, Nature, 533, 221
Gillon, M., Triaud, A. H. M. J., Demory, B.-O., et al. 2017, Nature, 542, 456
Goffo, E., Gandolfi, D., Egger, J. A., et al. 2023, ApJ, 955, L3
Goldreich, P., & Schlichting, H. E. 2014, AJ, 147, 32
Goldreich, P., & Soter, S. 1966, Icarus, 5, 375
Goldreich, P., & Tremaine, S. 1979, ApJ, 233, 857
Gondoin, P. 2020, A&A, 641, A110
González-Álvarez, E., Zapatero Osorio, M. R., Sanz-Forcada, J., et al. 2022, A&A, 658, A138

González Hernández, J. I., Suárez Mascareño, A., Silva, A. M., et al. 2024, A&A, 690, A79
Goodman, J., & Weare, J. 2010, Commun. Appl. Math. Comput. Sci., 5, 65
Grasset, O., Schneider, J., & Sotin, C. 2009, ApJ, 693, 722
Grieves, N., Bouchy, F., Ulmer-Moll, S., et al. 2022, A&A, 668, A29
Grieves, N., Bouchy, F., Armstrong, D. J., et al. 2025, A&A, 693, A144
Guenther, E. W., Goffo, E., Sebastian, D., et al. 2024, MNRAS, 529, 141
Hara, N. C., Boué, G., Laskar, J., & Correia, A. C. M. 2017, MNRAS, 464, 1220
Hara, N. C., Bouchy, F., Stalport, M., et al. 2020, A&A, 636, L6
Hara, N. C., Delisle, J.-B., Unger, N., & Dumusque, X. 2022, A&A, 658, A177
Haywood, R. D., Collier Cameron, A., Queloz, D., et al. 2014, MNRAS, 443, 2517
Heller, R., Hippke, M., & Rodenbeck, K. 2019, A&A, 627, A66
Hellier, C., Anderson, D. R., Collier Cameron, A., et al. 2012, MNRAS, 426, 739
Henden, A. A. 2019, jaavso, 47, 130
Henden, A. A., Templeton, M., Terrell, D., et al. 2016, VizieR On-line Data Catalog: II/336
Henry, T. J., Soderblom, D. R., Donahue, R. A., & Baliunas, S. L. 1996, AJ, 111, 439
Higson, E., Handley, W., Hobson, M., & Lasenby, A. 2019, Stat. Comput., 29, 891
Hippke, M., & Heller, R. 2019, A&A, 623, A39
Hippke, M., David, T. J., Mulders, G. D., & Heller, R. 2019, AJ, 158, 143
Hobson, M. J., Bouchy, F., Lavie, B., et al. 2024, A&A, 688, A216
Hon, M., Rappaport, S., Shporer, A., et al. 2025, ApJ, 984, L3
Howard, A. W., Marcy, G. W., Bryson, S. T., et al. 2012, ApJS, 201, 15
Howell, S. B., Sobeck, C., Haas, M., et al. 2014, PASP, 126, 398
Hsu, D. C., Ford, E. B., Ragozzine, D., & Ashby, K. 2019, AJ, 158, 109
Hu, R., Ehlmann, B. L., & Seager, S. 2012, ApJ, 752, 7
Huber, D., Bryson, S. T., Haas, M. R., et al. 2016, ApJS, 224, 2
Husser, T. O., Wende-von Berg, S., Dreizler, S., et al. 2013, A&A, 553, A6
Ioannidis, P., & Schmitt, J. H. M. M. 2016, A&A, 594, A41
Jackson, B., Stark, C. C., Adams, E. R., Chambers, J., & Deming, D. 2013, ApJ, 779, 165
Jackson, B., Jensen, E., Peacock, S., Arras, P., & Penev, K. 2016, Celest. Mech. Dyn. Astron., 126, 227
Jeffreys, H. 1961, The Theory of Probability, 3rd edn. (Oxford: Oxford University Press)
Jenkins, J. M., Twicken, J. D., McCauliff, S., et al. 2016, SPIE Conf. Ser., 9913, 99133E
Jia, S., & Spruit, H. C. 2017, MNRAS, 465, 149
John, A. A., Collier Cameron, A., Faria, J. P., et al. 2023, MNRAS, 525, 1687
Kipping, D. M. 2013, MNRAS, 435, 2152
Kite, E. S., & Barnett, M. N. 2020, Proc. Natl. Acad. Sci., 117, 18264
Kossakowski, D., Kemmer, J., Bluhm, P., et al. 2021, A&A, 656, A124
Kreidberg, L. 2015, PASP, 127, 1161
Kurucz, R. L. 1993, SYNTHE Spectrum Synthesis Programs and Line Data (Cambridge, Mass.: Smithsonian Astrophysical Observatory)
Lacedelli, G., Pallé, E., Luque, R., et al. 2024, A&A, 692, A238
Lai, D., Rasio, F. A., & Shapiro, S. L. 1993, ApJS, 88, 205
Lam, K. W. F., Csizmadia, S., Astudillo-Defru, N., et al. 2021, Science, 374, 1271
Lambeck, K. 1980, The Earth's Variable Rotation: Geophysical Causes and Consequences (Cambridge: Cambridge University Press)
Laskar, J. 1990, Icarus, 88, 266
Laskar, J. 1993, Phys. D Nonlinear Phenom., 67, 257
Laskar, J., & Robutel, P. 2001, Celest. Mech. Dyn. Astron., 80, 39
Lavie, B., Bouchy, F., Lovis, C., et al. 2023, A&A, 673, A69
Lee, E. J., & Chiang, E. 2017, ApJ, 842, 40
Lee, M. H., & Peale, S. J. 2002, ApJ, 567, 596
Leleu, A., Alibert, Y., Hara, N. C., et al. 2021, A&A, 649, A26
Lichtenberg, T., & Miguel, Y. 2025, Treat. Geochem., 7, 51
Lillo-Box, J., Figueira, P., Leleu, A., et al. 2020, A&A, 642, A121
Lin, D. N. C., Bodenheimer, P., & Richardson, D. C. 1996, Nature, 380, 606
Lissauer, J. J., Ragozzine, D., Fabrycky, D. C., et al. 2011, ApJS, 197, 8
Liu, F., Ting, Y.-S., Yong, D., et al. 2024, Nature, 627, 501
Livingston, J. H., Endl, M., Dai, F., et al. 2018, AJ, 156, 78
Lopez, E. D. 2017, MNRAS, 472, 245
Love, A. 1892, A Treatise on the Mathematical Theory of Elasticity (Cambridge: Cambridge University Press), 1
Lovis, C., Dumusque, X., Santos, N. C., et al. 2011, A&A, submitted [arXiv:1107.5325]
Luger, R., Agol, E., Kruse, E., et al. 2016, AJ, 152, 100
Luger, R., Kruse, E., Foreman-Mackey, D., Agol, E., & Saunders, N. 2018, AJ, 156, 99
Lundkvist, M. S., Kjeldsen, H., Albrecht, S., et al. 2016, Nat. Commun., 7, 11201
Luque, R., Osborn, H. P., Leleu, A., et al. 2023, Nature, 623, 932
Malavolta, L., Mayo, A. W., Louden, T., et al. 2018, AJ, 155, 107
Malhotra, R. 1993, Nature, 365, 819
Mamajek, E. E., & Hillenbrand, L. A. 2008, ApJ, 687, 1264
Mandel, K., & Agol, E. 2002, ApJ, 580, L171
Marcus, R. A., Sasselov, D., Hernquist, L., & Stewart, S. T. 2010, ApJ, 712, L73
Mardling, R. A. 2007, MNRAS, 382, 1768
Mardling, R. A. 2010, MNRAS, 407, 1048
Mayo, A. W., Vanderburg, A., Latham, D. W., et al. 2018, AJ, 155, 136
Mayor, M., Marmier, M., Lovis, C., et al. 2011, ArXiv e-prints [arXiv:1109.2497]
McArthur, B. E., Endl, M., Cochran, W. D., et al. 2004, ApJ, 614, L81
Middelkoop, F. 1982, A&A, 107, 31
Millholland, S. C., & Spalding, C. 2020, ApJ, 905, 71
Morello, G., Parviainen, H., Murgas, F., et al. 2023, A&A, 673, A32
Mortier, A., Zapatero Osorio, M. R., Malavolta, L., et al. 2020, MNRAS, 499, 5004
Morton, T. D. 2015, Astrophysics Source Code Library [record ascl:1503.010]
Morton, T. D., Bryson, S. T., Coughlin, J. L., et al. 2016, ApJ, 822, 86
Murgas, F., Castro-González, A., Pallé, E., et al. 2023, A&A, 677, A182
Murgas, F., Pallé, E., Orell-Miquel, J., et al. 2024, A&A, 684, A83
Mustill, A. J., Davies, M. B., & Johansen, A. 2015, ApJ, 808, 14
Noyes, R. W., Hartmann, L. W., Baliunas, S. L., Duncan, D. K., & Vaughan, A. H. 1984, ApJ, 279, 763
Ofir, A., & Dreizler, S. 2013, A&A, 555, A58
Oh, S., Price-Whelan, A. M., Brewer, J. M., et al. 2018, ApJ, 854, 138
Osborn, H. P., Nowak, G., Hébrard, G., et al. 2023, MNRAS, 523, 3069
Owen, J. E. 2019, Ann. Rev. Earth Planet. Sci., 47, 67
Parviainen, H., & Aigrain, S. 2015, MNRAS, 453, 3821
Passegger, V. M., Suárez Mascareño, A., Allart, R., et al. 2024, A&A, 684, A22
Patel, J. A., & Espinoza, N. 2022, AJ, 163, 228
Pearson, K. A. 2019, AJ, 158, 243
Pepe, F., Mayor, M., Galland, F., et al. 2002, A&A, 388, 632
Pepe, F., Cristiani, S., Rebolo, R., et al. 2021, A&A, 645, A96
Perot, A., & Fabry, C. 1899, ApJ, 9, 87
Peterson, M. S., Benneke, B., Collins, K., et al. 2023, Nature, 617, 701
Petrovich, C., Deibert, E., & Wu, Y. 2019, AJ, 157, 180
Polanski, A. S., Lubin, J., Beard, C., et al. 2024, ApJS, 272, 32
Pu, B., & Lai, D. 2019, MNRAS, 488, 3568
Ramírez, I., Khanal, S., Aleo, P., et al. 2015, ApJ, 808, 13
Rappaport, S., Levine, A., Chiang, E., et al. 2012, ApJ, 752, 1
Rappaport, S., Sanchis-Ojeda, R., Rogers, L. A., Levine, A., & Winn, J. N. 2013, ApJ, 773, L15
Rappaport, S., Barclay, T., DeVore, J., et al. 2014, ApJ, 784, 40
Rasmussen, C. E., & Williams, C. K. I. 2006, Gaussian Processes for Machine Learning (Cambridge: MIT Press)
Raymond, S. N., Mandell, A. M., & Sigurdsson, S. 2006, Science, 313, 1413
Ricker, G. R., Winn, J. N., Vanderspek, R., et al. 2014, SPIE Conf. Ser., 9143, 914320
Roberts, S., Osborne, M., Ebden, M., et al. 2012, Phil. Trans. R. Soc. London Ser. A, 371, 20110550
Rodgers, J. L., & Nicewander, W. A. 1988, Am. Stat., 42, 59
Rodrigues, J., Barros, S. C. C., Santos, N. C., et al. 2025, A&A, 695, A237
Sairam, L., & Triaud, A. H. M. J. 2022, MNRAS, 514, 2259
Sairam, L., Triaud, A. H. M. J., Baycroft, T. A., et al. 2024, MNRAS, 527, 2261
Sanchis-Ojeda, R., Rappaport, S., Winn, J. N., et al. 2013, ApJ, 774, 54
Sanchis-Ojeda, R., Rappaport, S., Winn, J. N., et al. 2014, ApJ, 787, 47
Sanchis-Ojeda, R., Rappaport, S., Pallè, E., et al. 2015, ApJ, 812, 112
Santerne, A., Brugger, B., Armstrong, D. J., et al. 2018, Nat. Astron., 2, 393
Santos, N. C., Israelian, G., & Mayor, M. 2001, A&A, 373, 1019
Santos, N. C., Sousa, S. G., Mortier, A., et al. 2013, A&A, 556, A150
Santos, N. C., Adibekyan, V., Mordasini, C., et al. 2015, A&A, 580, L13
Santos, N. C., Adibekyan, V., Dorn, C., et al. 2017, A&A, 608, A94
Schönrich, R., Binney, J., & Dehnen, W. 2010, MNRAS, 403, 1829
Shkolnik, E., Walker, G. A. H., Bohlender, D. A., Gu, P. G., & Kürster, M. 2005, ApJ, 622, 1075
Shkolnik, E. L., & Llama, J. 2018, in Handbook of Exoplanets, eds. H. J. Deeg & J. A. Belmonte (Berlin: Springer), 20
Shorttle, O., Jordan, S., Nicholls, H., Lichtenberg, T., & Bower, D. J. 2024, ApJ, 962, L8
Silva, A. M., Faria, J. P., Santos, N. C., et al. 2022, A&A, 663, A143
Silva, A. M., Santos, N. C., & Faria, J. P. 2025, A&A, in press, https://doi.org/10.1051/0004-6361/202554955
Siverd, R. J., Beatty, T. G., Pepper, J., et al. 2012, ApJ, 761, 123
Skrutskie, M. F., Cutri, R. M., Stiening, R., et al. 2006, AJ, 131, 1163
Smith, J. C., Stumpe, M. C., Van Cleve, J. E., et al. 2012, PASP, 124, 1000
Smith, A. M. S., Cabrera, J., Csizmadia, S., et al. 2018, MNRAS, 474, 5523
Sneden, C. A. 1973, PhD thesis, The University of Texas at Austin, USA
Soares, B. M. T. B., Adibekyan, V., Mordasini, C., et al. 2025, A&A, 693, A47

Sousa, S. G. 2014, in Determination of Atmospheric Parameters of B, eds. E. Niemczura, B. Smalley, & W. Pych (Berlin: Springer), 297
Sousa, S. G., Santos, N. C., Israelian, G., Mayor, M., & Monteiro, M. J. P. F. G. 2007, A&A, 469, 783
Sousa, S. G., Santos, N. C., Mayor, M., et al. 2008, A&A, 487, 373
Sousa, S. G., Santos, N. C., Adibekyan, V., Delgado-Mena, E., & Israelian, G. 2015, A&A, 577, A67
Sousa, S. G., Adibekyan, V., Delgado-Mena, E., et al. 2021, A&A, 656, A53
Sozzetti, A., Torres, G., Charbonneau, D., et al. 2007, ApJ, 664, 1190
Sozzetti, A., Damasso, M., Bonomo, A. S., et al. 2021, A&A, 648, A75
Speagle, J. S. 2020, MNRAS, 493, 3132
Standing, M. R., Triaud, A. H. M. J., Faria, J. P., et al. 2022, MNRAS, 511, 3571
Standing, M. R., Sairam, L., Martin, D. V., et al. 2023, Nat. Astron., 7, 702
Stassun, K. G., Oelkers, R. J., Pepper, J., et al. 2018, AJ, 156, 102
Stumpe, M. C., Smith, J. C., Van Cleve, J. E., et al. 2012, PASP, 124, 985
Suárez Mascareño, A., Rebolo, R., & González Hernández, J. I. 2016, A&A, 595, A12
Suárez Mascareño, A., Rebolo, R., González Hernández, J. I., & Esposito, M. 2017, MNRAS, 468, 4772
Suárez Mascareño, A., Faria, J. P., Figueira, P., et al. 2020, A&A, 639, A77
Suárez Mascareño, A., Passegger, V. M., González Hernández, J. I., et al. 2024, A&A, 685, A56
Szabó, G. M., & Kiss, L. L. 2011, ApJ, 727, L44
Tian, M., & Heng, K. 2024, ApJ, 963, 157
Tikoo, S. M., & Elkins-Tanton, L. T. 2017, Phil. Trans. R. Soc. London Ser. A, 375, 20150394
Toledo-Padrón, B., Lovis, C., Suárez Mascareño, A., et al. 2020, A&A, 641, A92
Tremaine, S., & Dong, S. 2012, AJ, 143, 94
Turbet, M., Bolmont, E., Ehrenreich, D., et al. 2020, A&A, 638, A41
Vanderburg, A., & Johnson, J. A. 2014, PASP, 126, 948
Vaughan, A. H., & Preston, G. W. 1980, PASP, 92, 385
Vissapragada, S., & Behmard, A. 2025, AJ, 169, 117
Weiss, L. M., Marcy, G. W., Rowe, J. F., et al. 2013, ApJ, 768, 14
Wells, R., Poppenhaeger, K., & Watson, C. A. 2018, MNRAS, 473, L131
Wildi, F., Pepe, F., Chazelas, B., Lo Curto, G., & Lovis, C. 2010, SPIE Conf. Ser., 7735, 77354X
Winn, J. N., Sanchis-Ojeda, R., Rogers, L., et al. 2017, AJ, 154, 60
Winn, J. N., Sanchis-Ojeda, R., & Rappaport, S. 2018, New A Rev., 83, 37
Wong, I., Shporer, A., Zhou, G., et al. 2021, AJ, 162, 256
Wu, Y., & Goldreich, P. 2002, ApJ, 564, 1024
Wu, Y., & Lithwick, Y. 2011, ApJ, 735, 109
Wu, Y., & Murray, N. 2003, ApJ, 589, 605
Yoder, C. F. 1995, in Global Earth Physics: A Handbook of Physical Constants, ed. T. J. Ahrens (Washington, D.C.: American Geophysical Union), 1
Youdin, A. N. 2011, ApJ, 742, 38
Zacharias, N., Finch, C. T., Girard, T. M., et al. 2013, AJ, 145, 44
Zechmeister, M., & Kürster, M. 2009, A&A, 496, 577
Zeng, L., Sasselov, D. D., & Jacobsen, S. B. 2016, ApJ, 819, 127
Zeng, L., Jacobsen, S. B., Sasselov, D. D., et al. 2019, Proc. Natl. Acad. Sci., 116, 9723
Zhang, M., Hu, R., Inglis, J., et al. 2024, ApJ, 961, L44

[1] Centro de Astrobiología, CSIC-INTA, Camino Bajo del Castillo s/n, 28692 Villanueva de la Cañada, Madrid, Spain
[2] Observatoire de l'Université de Genève, 51 chemin Pegasi, 1290 Sauverny, Switzerland
[3] Département d'Astronomie, Université de Genève, Chemin Pegasi 51, 1290 Versoix, Switzerland
[4] CFisUC, Departamento de Física, Universidade de Coimbra, 3004-516 Coimbra, Portugal
[5] IMCCE, UMR8028 CNRS, Observatoire de Paris, PSL Université, 77 Av. Denfert-Rochereau, 75014 Paris, France
[6] INAF - Osservatorio Astrofisico di Torin, Via Osservatorio 20, 10025 Pino Torinese, Italy
[7] Instituto de Astrofísica e Ciências do Espaço, Universidade do Porto, CAUP, Rua das Estrelas, 4150-762 Porto, Portugal
[8] Departamento de Fisica e Astronomia, Universidade do Porto, Rua do Campo Alegre, 4169-007 Porto, Portugal
[9] European Space Agency (ESA), European Space Astronomy Centre (ESAC), Camino Bajo del Castillo s/n, 28692 Villanueva de la Cañada, Madrid, Spain
[10] Université Aix Marseille, CNRS, CNES, LAM, Marseille, France
[11] Instituto de Astrofísica e Ciências do Espaço, Universidade de Lisboa, Campo Grande, 1749-016 Lisboa, Portugal
[12] Lund Observatory, Division of Astrophysics, Department of Physics, Lund University, Box 118, 22100 Lund, Sweden
[13] Observatoire François-Xavier Bagnoud – OFXB, 3961 Saint-Luc, Switzerland
[14] Center for Space and Habitability, University of Bern, Gesellschaftsstrasse 6, 3012 Bern, Switzerland
[15] Physics Institute of University of Bern, Gesellschaftsstrasse 6, 3012 Bern, Switzerland
[16] INAF – Osservatorio Astronomico di Trieste, via G. B. Tiepolo 11, 34143 Trieste, Italy
[17] Instituto de Astrofísica de Canarias, 38205 La Laguna, Tenerife, Spain
[18] Universidad de La Laguna, Dept. Astrofísica, 38206 La Laguna, Tenerife, Spain
[19] European Southern Observatory, Av. Alonso de Cordova 3107, Casilla 19001, Santiago de Chile, Chile
[20] Centro de Astrofísica da Universidade do Porto, Rua das Estrelas, 4150-762 Porto, Portugal
[21] Département d'Astronomie, Université de Genève, Ch. des Maillettes 51, 1290 Versoix, Switzerland
[22] Institut de Ciències de l'Espai (ICE, CSIC), Campus UAB, c/ de Can Magrans s/n, 08193 Cerdanyola del Vallès, Barcelona, Spain
[23] Institut d'Estudis Espacials de Catalunya (IEEC), Edifici RDIT, Campus UPC, 08860 Castelldefels (Barcelona), Spain

Appendix A: Additional figures

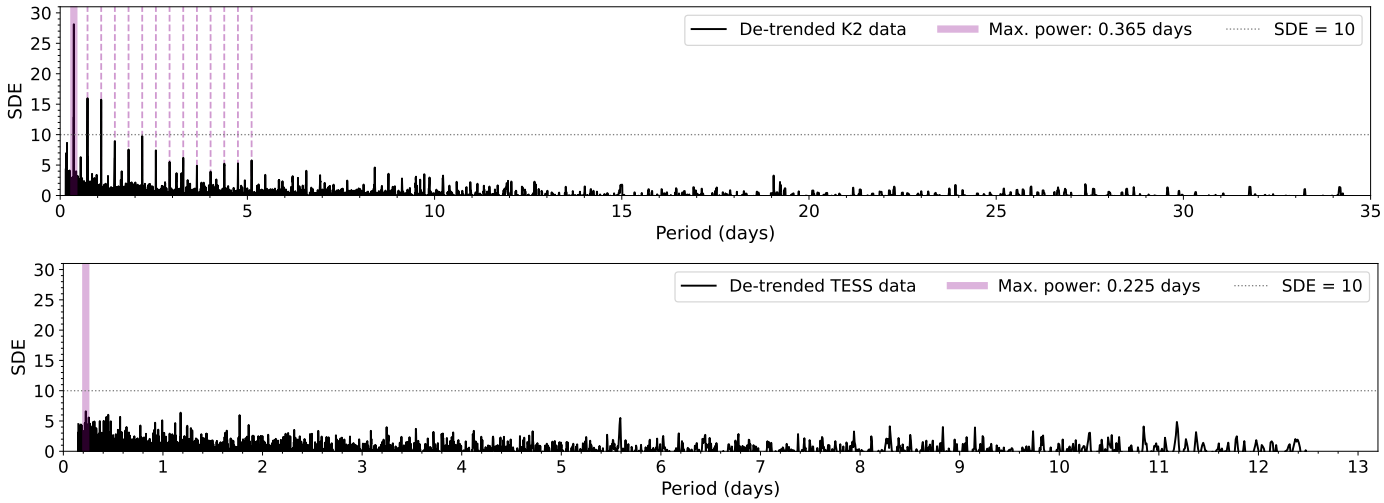


Fig. A.1. Transit least squares (TLS) periodogram of the K2 (C10) and TESS (S46) photometry of K2-157 detrended with the bi-weight technique considering a window length of 0.5 d. The horizontal dotted lines indicate a conservative threshold for considering a significant transit detection. The vertical dashed lines indicate the first harmonics of the maximum power period (0.365 d).

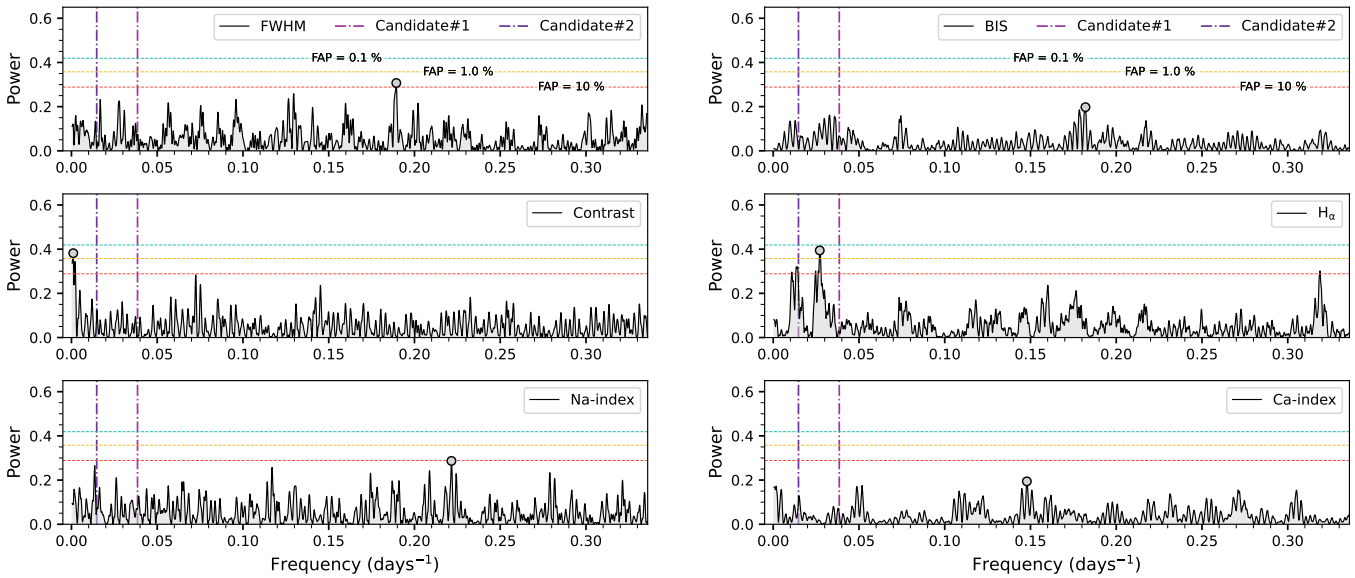


Fig. A.2. Generalized Lomb-Scargle periodograms (GLS) of the ESPRESSO activity indicators of K2-157. The grey circles indicate the maximum power frequencies. The vertical dash-dotted lines indicate the frequencies of the sinusoidal periodicities of Candidate#1 and Candidate#2. The horizontal dotted lines show the 10%, 1%, and 0.1% FAP levels.

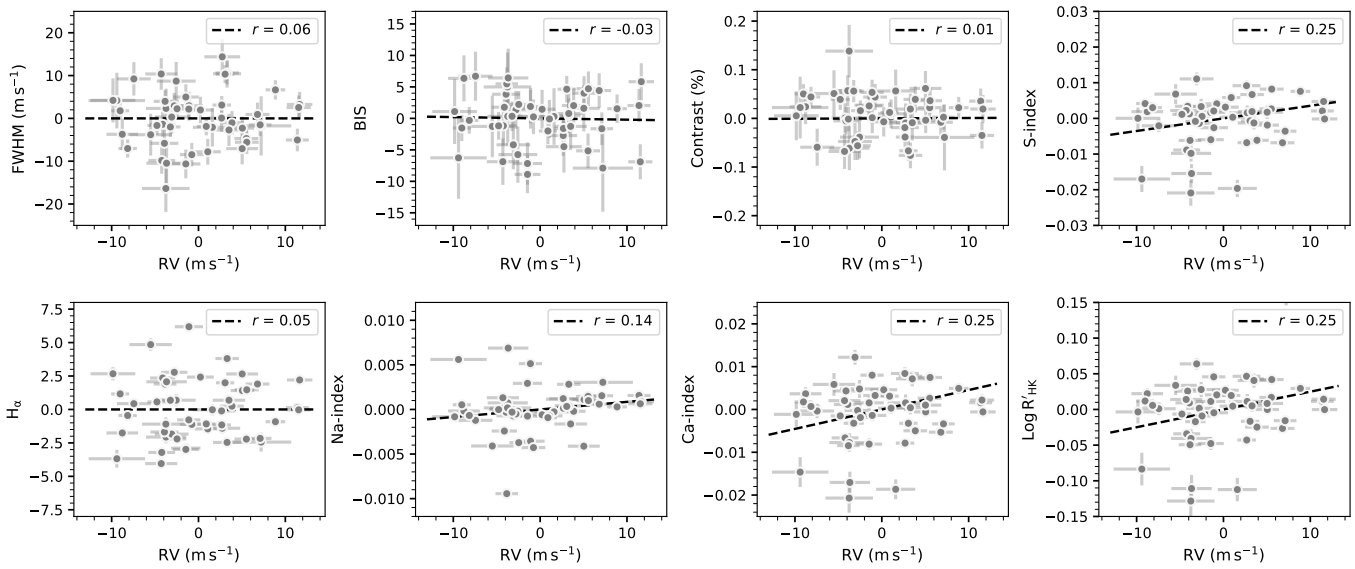


Fig. A.3. ESPRESSO activity indicators as a function of the RVs of K2-157. The dashed lines represent linear trends fitted to the data. The legends indicate the Pearson product-moment correlation coefficients r.

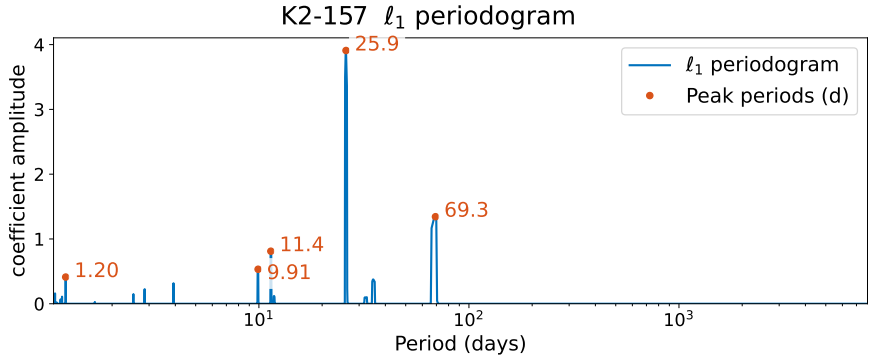


Fig. A.4. ℓ_1 periodogram of the ESPRESSO RVs, assuming a quadratic trend, and a covariance model selected with highest Bayesian evidence, computed with the Laplace approximation.

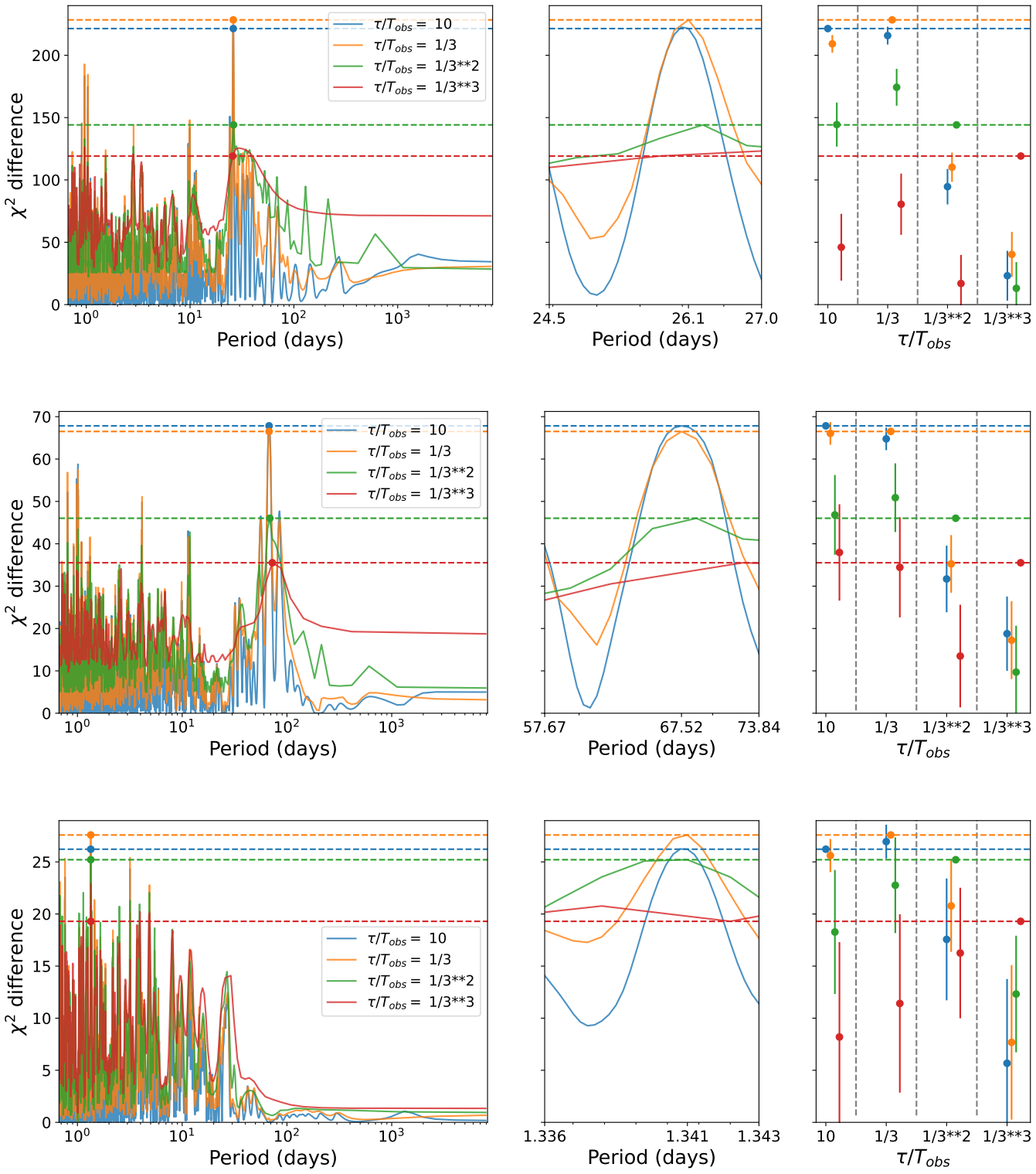


Fig. A.5. First three iterations of the apodized sine periodograms (ASPs) method. Models correspond to the maximum of the ASPs. $T_{\rm obs}$ designates the timespan between the first and last RV observation, and τ has the same meaning as in Eq. (1). The left panels represent the periodograms, the middle panels show a zoom in on the highest peak, and the right-hand panels represent a statistical significance test (see Hara et al. 2022, for details). We note that the best fitting τ for the 26 d signal is not the longest. We attribute this to the sequential fitting. In the first iteration, the 69 d signal is not removed. Because there are only 49 RV measurements, the aliasing is strong, and the presence of the 69 d signal in the first iteration creates interferences. If we first remove the 69 d signal, the longest timescale has the same statistical significance as $\tau/T_{\rm obs} = 3$.

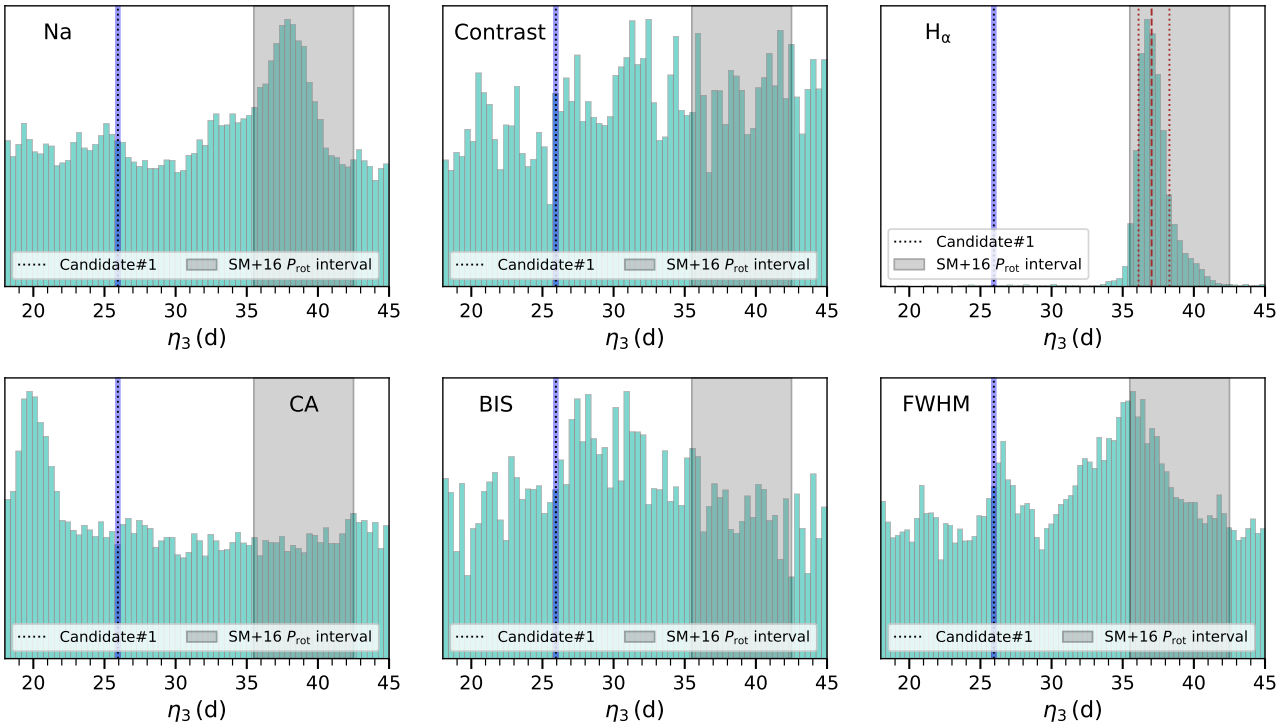


Fig. A.6. Posterior distribution of the η_3 hyperparameter of the quasiperiodic GP kernel used to describe the ESPRESSO activity indicators (Sect. 4.3). The vertical dash-dotted black line indicates the orbital period of Candidate#1 and the vertical blue shade indicates its 3σ confidence interval. The vertical grey shade represents the 1σ confidence interval of the expected $P_{\rm rot}$, inferred through the $\log(R'_{\rm HK})$-$P_{\rm rot}$ relations from Suárez Mascareño et al. (2016). In the H_α panel, the vertical dashed and dotted brown lines indicate the median value and the 1σ confidence intervals of the distribution, respectively ($\eta_{3,{\rm H}_\alpha} = 37.03^{+1.25}_{-0.92}$ d).

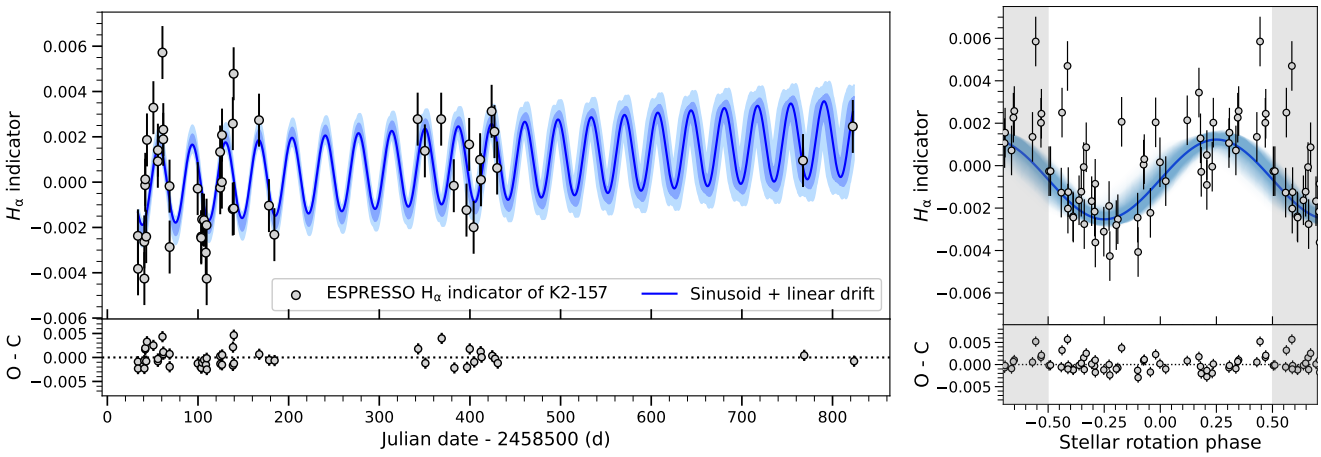


Fig. A.7. ESPRESSO H_α indicator of K2-157. The solid line represents the median posterior sinusoidal model, and the dark and light shades represent the 1σ and 3σ confidence intervals, respectively. The left panel contains the full data set, and the right panel contains the H_α data folded to the inferred periodicity ($P_{{\rm rot},{\rm H}_\alpha} = 36.76^{+0.40}_{-0.44}$ d).

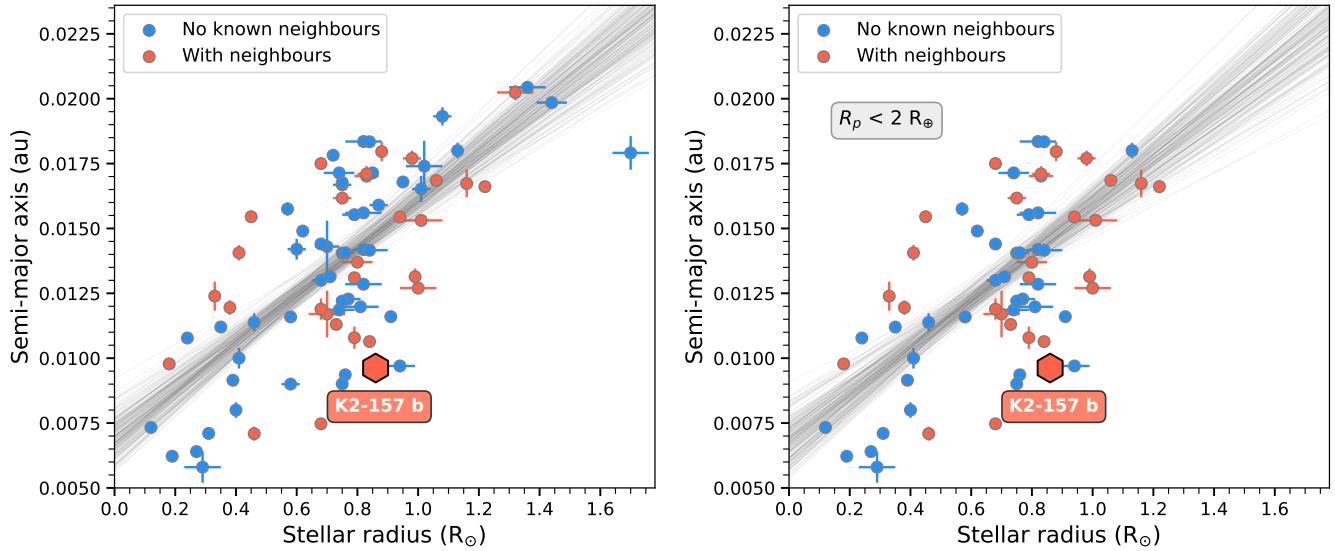


Fig. A.8. Semi-major axis versus stellar radius of all USP planets (left) and of a restricted sample with $R_p < 2\ R_\oplus$ (right). Planets without reported neighbours are coloured in blue, while those with known neighbours a coloured in orange. The straight grey lines are 200 random posterior linear models (i.e. $Ax + B$). Data: NASA Exoplanet Archive (24/03/2025).

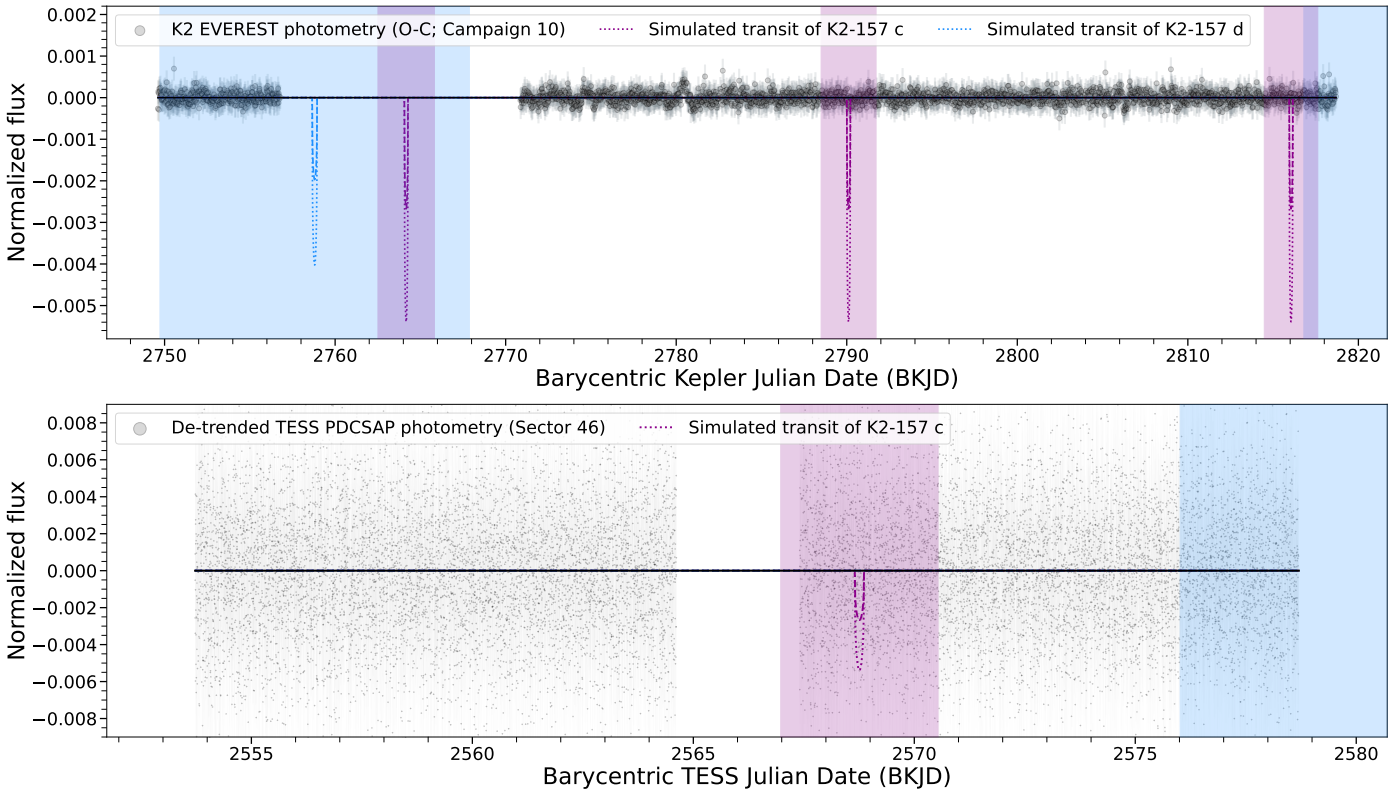


Fig. A.9. Predicted transit times of K2-157 c and K2-157 d along the K2 (C10, upper panel) and TESS (S46, lower panel) observing baselines, obtained from our RV-derived ephemeris (Table B.5). Shaded regions represent the 1σ confidence intervals. The dotted (dashed) simulated transits assume the median (1σ lower limit) $R_p/R_\star$ as estimated by `forecaster` (Chen & Kipping 2017).

Appendix B: Additional tables

Table B.1. K2 `everest` photometry of K2-157. The complete table is available at the CDS.

BJD (days)	FLUX	FLUX_ERR	Campaign
2457582.6106	0.9997	0.0003	C10
2457582.6310	1.0001	0.0003	C10
...	...	...	...

Table B.2. TESS PDCSAP photometry of K2-157. The complete table is available at the CDS.

BJD (days)	FLUX	FLUX_ERR	Sector
2459553.7278	0.9974	0.0044	S46
2459553.7291	0.9995	0.0044	S46
...	...	...	...

Table B.3. ESPRESSO RVs and activity indicators of K2-157 acquired between 19 February 2019 and 19 April 2021 under the programmes with IDs 1102.C-0744, 1102.C-0958, 1104.C-0350, and 106.21M2.004. The complete table is available at the CDS.

BJD (days)	RV_{DRS} ($m\,s^{-1}$)	RV_{sbart} ($m\,s^{-1}$)	FWHM	BIS	Contrast	H_α	Na-index	Ca-index
2458533.7351	43436.9 ± 1.8	43439.7 ± 1.8	6413.4 ± 3.7	-60.5 ± 3.7	62.820 ± 0.036	0.20662 ± 0.00036	0.22297 ± 0.00026	0.1372 ± 0.0015
2458533.8509	43441.4 ± 1.5	43438.8 ± 1.8	6407.2 ± 3.1	-68.0 ± 3.1	62.797 ± 0.030	0.20517 ± 0.00030	0.22328 ± 0.00021	0.1269± 0.0011
...	...	...	...	...	...	...	...	...

Table B.4. Parameters of K2-157 c and K2-157 d based on the ESPRESSO blind-search analysis described in Sect. 4.2.

Parameter	Priors	Posteriors
Orbital and physical parameters of K2-157 c		
Orbital period, $P_{orb,c}$ (days)	$\mathcal{U}(0, 400)$	$25.968^{+0.051}_{-0.052}$
Time of mid-transit, $T_{0,c}$ (JD)	$\mathcal{U}(2458533, 2458933)$	2458557.03 ± 0.36
RV semi-amplitude, K_c ($m\,s^{-1}$)	$\mathcal{U}(0, 20)$	7.10 ± 0.49
Minimum mass, $M_{p,c} \sin i$ ($M_\oplus$)	(derived)	30.4 ± 2.2
Minimum mass, $M_{p,c} \sin i$ (M_J)	(derived)	0.0958 ± 0.0069
Relative orbital separation, $a_c/R_\star$	(derived)	41.3 ± 1.0
Orbit semi-major axis, a_c (au)	(derived)	0.1651 ± 0.0018
Incident flux, $F_{inc,c}$ ($F_\oplus$)	(derived)	22.62 ± 0.68
Equilibrium temperature [A=0], $T_{eq,c}$ (K)	(derived)	587 ± 10
Orbital and physical parameters of K2-157 d		
Orbital period, $P_{orb,d}$ (days)	$\mathcal{U}(0, 400)$	$66.62^{+0.99}_{-0.75}$
Time of mid-transit, $T_{0,d}$ (JD)	$\mathcal{U}(2458533, 2458933)$	$2458588.9^{+2.2}_{-2.8}$
RV semi-amplitude, K_d ($m\,s^{-1}$)	$\mathcal{U}(0, 20)$	$3.79^{+0.49}_{-0.48}$
Minimum mass, $M_{p,d} \sin i$ ($M_\oplus$)	(derived)	22.3 ± 2.8
Minimum mass, $M_{p,d} \sin i$ (M_J)	(derived)	0.0701 ± 0.0089
Relative orbital separation, $a_d/R_\star$	(derived)	77.4 ± 2.0
Orbit semi-major axis, a_d (au)	(derived)	0.3093 ± 0.0041
Incident flux, $F_{inc,d}$ ($F_\oplus$)	(derived)	6.44 ± 0.22
Equilibrium temperature [A=0], $T_{eq,d}$ (K)	(derived)	429 ± 8
RV jitter and quadratic trend		
RV jitter, σ_{jit} ($m\,s^{-1}$)	$\mathcal{U}(0, 10)$	$1.43^{+0.35}_{-0.39}$
Systemic velocity, v_{sys} ($m\,s^{-1}$)	$\mathcal{U}(43430, 43460)$	$43448.00^{+0.79}_{-0.83}$
Linear term, γ ($m\,s^{-1}\,day^{-1}$)	$\mathcal{U}(-0.1, 0.1)$	$-0.0498^{+0.0062}_{-0.0061}$
Quadratic term, δ ($m\,s^{-1}\,day^{-2}$)	$\mathcal{U}(-0.01, 0.01)$	$6.5 \pm 1.1 \times 10^{-5}$

Table B.5. Parameters of K2-157 b, K2-157 c, and K2-157 d based on the joint fit analysis described in Sect. 4.4.

Parameter	Priors	Posteriors
Orbital and physical parameters of K2-157 b		
Orbital period, $P_{\rm orb,b}$ (days)	$\mathcal{U}(0.3, 0.4)$	$0.3652575^{+0.0000078}_{-0.0000088}$
Time of mid-transit, $T_{0,\rm b}$ (JD)	$\mathcal{U}(2457582.6, 2457583.0)$	$2457582.8220^{+0.0041}_{-0.0032}$
Orbital inclination, $i_{\rm b}$ (degrees)	$\mathcal{U}(50, 150)$	$89.2^{+9.3}_{-9.1}$
Scaled planet radius, $R_{\rm p,b}/R_\star$	$\mathcal{U}(0.00, 0.05)$	0.00996 ± 0.00094
RV semi-amplitude, $K_{\rm b}$ (m s^{-1})	$\mathcal{U}(0, 20)$	$1.10^{+0.39}_{-0.41}$
Planet radius, $R_{\rm p,b}$ ($R_\oplus$)	(derived)	0.935 ± 0.090
Planet radius, $R_{\rm p,b}$ ($R_{\rm J}$)	(derived)	0.0834 ± 0.0081
Planet mass, $M_{\rm p,b}$($M_\oplus$)	(derived)	$1.14^{+0.41}_{-0.42}$
Planet mass, $M_{\rm p,b}$($M_{\rm J}$)	(derived)	0.0036 ± 0.0013
Planet density, $\rho_{\rm p,b}$ (g cm^{-3})	(derived)	7.7 ± 3.6
Transit depth, $\Delta_{\rm b}$ (ppm)	(derived)	99 ± 19
Transit duration, $T_{14,\rm b}$ (hours)	(derived)	1.161 ± 0.032
Relative orbital separation, $a_{\rm b}/R_\star$	(derived)	2.405 ± 0.059
Orbit semi-major axis, $a_{\rm b}$ (au)	(derived)	0.00962 ± 0.00010
Planet surface gravity, $g_{\rm b}$ (m s^{-2})	(derived)	12.8 ± 5.3
Impact parameter, $b_{\rm b}$	(derived)	0.03 ± 0.38
Incident flux, $F_{\rm inc,b}$ ($F_\oplus$)	(derived)	$(6.66 \pm 0.20) \times 10^3$
Equilibrium temperature [A=0], $T_{\rm eq,b}$ (K)	(derived)	2432 ± 42
Orbital and physical parameters of K2-157 c		
Orbital period, $P_{\rm orb,c}$ (days)	$\mathcal{U}(0, 400)$	$25.942^{+0.045}_{-0.044}$
Time of mid-transit, $T_{0,\rm c}$ (JD)	$\mathcal{U}(2458533, 2458933)$	2458557.02 ± 0.30
RV semi-amplitude, $K_{\rm c}$ (m s^{-1})	$\mathcal{U}(0, 20)$	7.17 ± 0.42
Minimum mass, $M_{\rm p,c} \sin i$ ($M_\oplus$)	(derived)	30.8 ± 1.9
Minimum mass, $M_{\rm p,c} \sin i$ ($M_{\rm J}$)	(derived)	0.0967 ± 0.0060
Relative orbital separation, $a_{\rm c}/R_\star$	(derived)	41.2 ± 1.0
Orbit semi-major axis, $a_{\rm c}$ (au)	(derived)	0.1650 ± 0.0018
Incident flux, $F_{\rm inc,c}$ ($F_\oplus$)	(derived)	22.65 ± 0.68
Equilibrium temperature [A=0], $T_{\rm eq,c}$ (K)	(derived)	587 ± 10
Orbital and physical parameters of K2-157 d		
Orbital period, $P_{\rm orb,d}$ (days)	$\mathcal{U}(0, 400)$	$66.50^{+0.71}_{-0.59}$
Time of mid-transit, $T_{0,\rm d}$ (JD)	$\mathcal{U}(2458533, 2458933)$	$2458589.3^{+1.7}_{-2.0}$
RV semi-amplitude, $K_{\rm d}$ (m s^{-1})	$\mathcal{U}(0, 20)$	$3.96^{+0.42}_{-0.41}$
Minimum mass, $M_{\rm p,d} \sin i$ ($M_\oplus$)	(derived)	23.3 ± 2.5
Minimum mass, $M_{\rm p,d} \sin i$ ($M_{\rm J}$)	(derived)	0.0732 ± 0.0077
Relative orbital separation, $a_{\rm d}/R_\star$	(derived)	77.3 ± 2.0
Orbit semi-major axis, $a_{\rm d}$ (au)	(derived)	0.3090 ± 0.0038
Incident flux, $F_{\rm inc,d}$ ($F_\oplus$)	(derived)	6.46 ± 0.21
Equilibrium temperature [A=0], $T_{\rm eq,d}$ (K)	(derived)	429.1 ± 7.5
RV quadratic trend		
Systemic velocity, $v_{\rm sys}$ (m s^{-1})	$\mathcal{U}(43430, 43460)$	$43448.11^{+0.64}_{-0.66}$
Linear term, γ (m s^{-1} day^{-1})	$\mathcal{U}(-0.1, 0.1)$	$-0.0491^{+0.0052}_{-0.0051}$
Quadratic term, δ (m s^{-1} day^{-2})	$\mathcal{U}(-0.01, 0.01)$	$6.20^{+0.92}_{-0.94} \times 10^{-5}$
Instrument-dependent parameters		
K2 LC level C10, $F_{0,\rm C10}$	$\mathcal{U}(-0.1, 0.1)$	$-0.000042^{+0.000216}_{-0.000233}$
K2 LC jitter C10, $\sigma_{\rm K2,C10}$	$\mathcal{U}(0, 0.005)$	$4.6^{+4.8}_{-3.2} \times 10^{-6}$
RV jitter, $\sigma_{\rm jit}$	$\mathcal{U}(0, 10)$	$1.06^{+0.38}_{-0.43}$
Limb-darkening coefficients		
Limb-darkening coefficient, $q_{1,\rm Kepler}$	$\mathcal{U}(0, 1)$	$0.62^{+0.26}_{-0.34}$
Limb-darkening coefficient, $q_{2,\rm Kepler}$	$\mathcal{U}(0, 1)$	$0.45^{+0.33}_{-0.30}$
GP hyperparameters		
η_σ	$\mathcal{U}(0, 0.5)$	$0.00048^{+0.00031}_{-0.00015}$
η_ρ (days)	$\mathcal{U}(0, 30)$	$6.3^{+3.1}_{-1.8}$

Appendix C: Corner plots

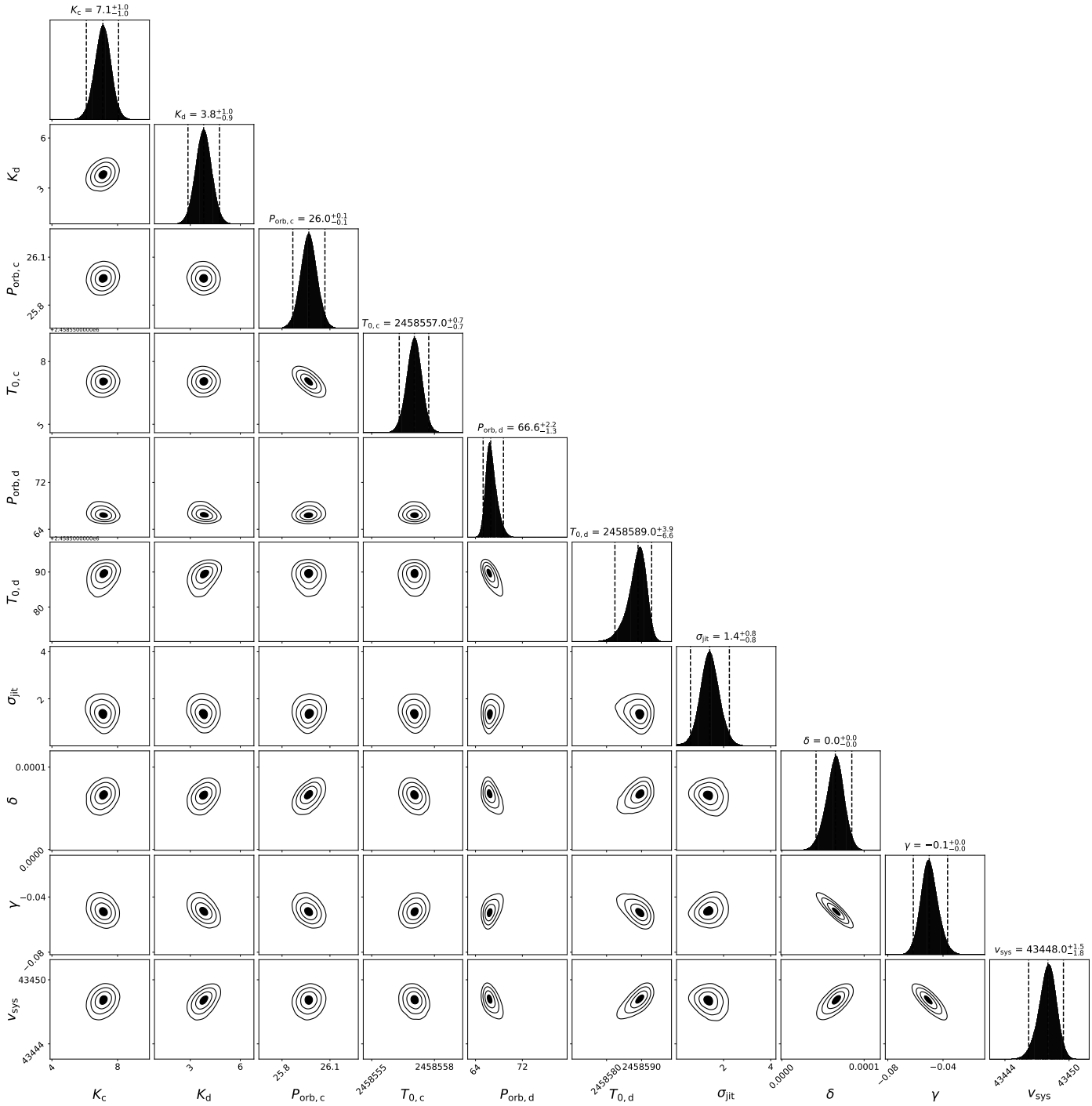


Fig. C.1. Corner plot with the 1D and 2D posterior distributions of the parameters of the model that best describes the RVs: 2p1c2cQ (i.e. 2 planets with circular orbits plus a quadratic trend; see Sect. 4.2). The vertical lines indicate the median and 2σ intervals.

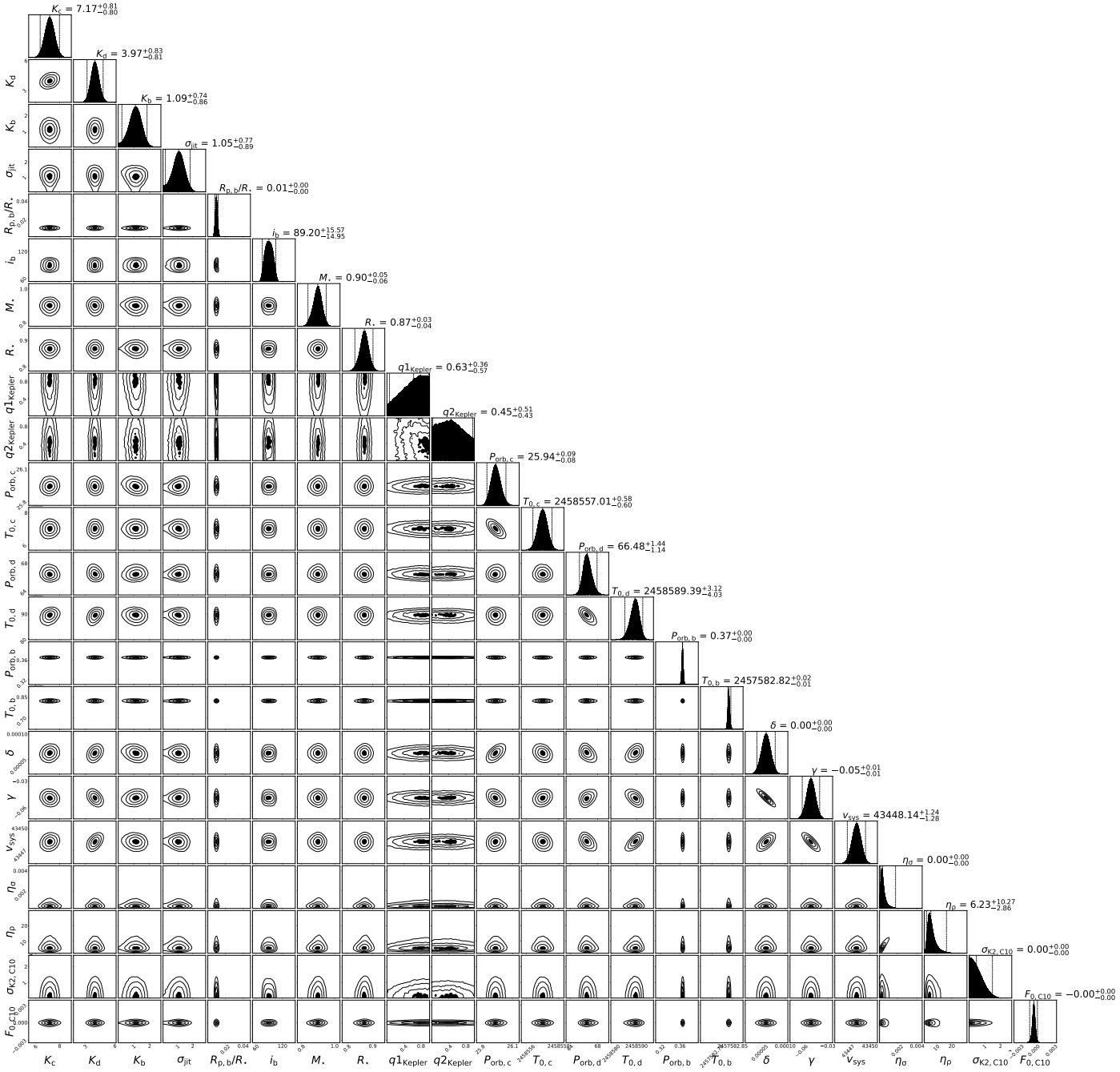


Fig. C.2. Corner plot with the 1D and 2D posterior distributions of the parameters of the global model (transit + RV) used in the joint fit analysis (see Sect. 4.4). The vertical lines indicate the median and 2σ intervals.